Angles-Only Navigation in the Proximity of a Binary Asteroid System

Francesco Torre*, Stuart Grey† and Massimiliano Vasile‡
University of Strathclyde, Glasgow, UK, G11XJ

This paper investigates the possibility to navigate one or more spacecraft in the proximity of an asteroid binary system using only optical measurements. The approach proposed in this paper assumes only limited prior knowledge of the shape and orbital parameters of the two asteroids. In particular it is shown that the knowledge of the semi-major axis of the orbit of the secondary with respect to the primary is critical to guarantee a sufficient level of navigation accuracy. A method is proposed to allow for the inclusion of the orbital parameters of the secondary asteroid in the estimation process. It is shown that the inclusion of the estimation of the orbital parameters of the secondary provides the required information to allow navigating in the proximity of the binary system at the Lagrange point L4. The paper then demonstrates that the same method can be used to navigate a small formation of two spacecraft at L4 provided that intersatellite position and velocity vectors can be measured with sufficient accuracy. In this case the formation can be controlled even if the optical sensor on board one of the spacecraft partially fails.

Nomenclature

A	=	primary asteroid
A_i	=	cross sectional area of spacecraft i, m^2
a_i	=	semi-axis along the x-axis of the body fixed frame of body i, km
a_{SRP_i}	=	acceleration vector due to the solar radiation pressure (SRP) on spacecraft i, km/s^2
B	=	secondary asteroid
b_i	=	semi-axis along the y-axis of the body fixed frame of body i, km
C	=	camera coordinate system
${}^kC_{ij}$	=	spherical harmonics coefficient of degree i and order j for body k, km^2

*PhD Student, Aerospace Centre of Excellence, Department of Mechanical and Aerospace Engineering, James Weir Building, Glasgow, G1 1XJ, AIAA Student Member
†Teaching Fellow, Aerospace Centre of Excellence, Department of Mechanical and Aerospace Engineering, James Weir Building, Glasgow, G1 1XJ, AIAA Student Member.
‡Professor, Aerospace Centre of Excellence, Department of Mechanical and Aerospace Engineering, James Weir Building, Glasgow, G1 1XJ, AIAA Student Member.

c_i = semi-axis along the z-axis of the body fixed frame of body i, km

d_r = distance between two spacecraft, km

f = generic function for dynamics

f_C = focal length of the camera

h = generic measurement function

K_d = derivative coefficient of PD controller, s^{-1}

K_p = proportional coefficient of PD controller, s^{-2}

k_{UHF} = filter tuning parameter

m_i = mass of body i, kg

n = length of the estimated state

$\mathbf{P}_k$ = estimated covariance matrix at time t_k

$\mathbf{P}_{k|k-1}$ = predicted covariance matrix at time t_k

$\mathbf{P}^{yy}_{k|k-1}$ = predicted measurements covariance matrix at time t_k

$\mathbf{P}^{xy}_{k|k-1}$ = predicted cross correlation covariance matrix at time t_k

$\mathbf{Q}$ = navigation dynamics weight matrix

$\mathbf{R}$ = measurements weight matrix

${}^{i}\mathbf{R}_j$ = rotation matrix from reference frame j to frame i

$\mathbf{r}_i$ = position vector of body i in the principal reference frame, km

$\mathbf{r}_{ij}$ = relative position vector from body i to j in the principal reference frame, km

S_{SRP} = solar radiation pressure at 1 AU, Pa

SC = spacecraft body-fixed coordinate system

t = time, h

${}^{k}U_{ij}$ = gravitational potential of degree i and order j for body k, km^2/s^2

$\mathbf{u}_i$ = control vector of spacecraft i, km/s^2

${}^{j}u_i$ = control vector component of spacecraft i in the direction j, km/s^2

$\mathbf{V}_{ij}$ = pointing vector from camera on spacecraft i looking at asteroid j to asteroid j

$\mathbf{v}_k$ = measurement noise vector at time t_k

X, Y, Z = axes of the principal reference frame

$\hat{X}_i, \hat{Y}_i, \hat{Z}_i$ = axes of the body-fixed frame on body i

$\tilde{\mathbf{x}}_k$ = estimated state at time t_k

$\hat{\mathbf{x}}_{k|k-1}$ = mean predicted state vector

$\hat{\mathbf{y}}_{k|k-1}$ = mean predicted measurement vector

${}^{P}\mathbf{y}_{ij}$	=	pointing measurement from spacecraft i to asteroid j
${}^{R}\mathbf{y}_{ij}$	=	relative position measurement from spacecraft i to spacecraft j in Cartesian coordinates
${}^{T}\mathbf{y}_{i}$	=	triangulation measurement for spacecraft i
x_{ij}, y_{ij}, z_{ij}	=	coordinates of spacecraft j in the body frame of i, km
$\mathbf{W}$	=	vector of weights used by the filter
$\mathbf{z}_r$	=	measurement vector of the relative position between the spacecraft, km
α_{UHF}	=	filter tuning parameter
α_{ij}	=	complementary angle to π of angle β_{ij}, rad
β_{ij}	=	angle between the pointing vector from spacecraft i to asteroid j and the baseline between asteroid A and B, rad
γ^2	=	filter parameter
$\delta\mathbf{r}_{ij}$	=	relative position vector between body i and s/c j in the body-fixed frame of i, km
ζ_r	=	noise vector of the measurement $\mathbf{z}_r$
μ_i	=	gravitational parameter of asteroid i, km^3/s^2
ρ_{ij}	=	relative position measurement from spacecraft i to spacecraft j in spherical coordinates
ϕ_r	=	azimuth of the measurement vector $\mathbf{z}_r$, rad
ψ_r	=	elevation of the measurement vector $\mathbf{z}_r$, rad
φ_{ij}	=	latitude of spacecraft j in the body frame of i, rad
θ_{ij}	=	longitude of spacecraft j in the body frame of i, rad
χ_k^i	=	i-th sigma point
$\chi_{k\|k-1}^i$	=	propagated i-th sigma point at time t_k
ω_i	=	angular velocity of asteroid i, rad/s

I. Introduction

The last two decades have seen an increasing interest in the exploration of the minor bodies of our solar system. Missions like NEAR, Hayabusa, Rosetta, Stardust and Dawn[1], to name a few, have fundamentally improved our knowledge of asteroids and comets. The JAXA mission Hayabusa2, visiting 162173 Ryugu, and NASA's OSIRIS-REx, collecting samples on 101955 Bennu, are continuing this challenging exploration of our solar system. Looking ahead ESA is planning to send the probe Hera to the binary asteroid 65803 Didymos in a joint mission with NASA, named AIDA. It is estimated that binary asteroids represent about 15% of the population of asteroids in the solar system and that they represent better candidates than single bodies to investigate effects such as Yarkovsky and YORP, and also to assess our technological capabilities in deflecting potentially hazardous objects (PHAs) [2] [3].

The interest in the exploration of asteroids and comets has led many authors to study and develop navigation systems

for close proximity operations around minor bodies with different levels of autonomy. From the navigation of the Rosetta mission[4, 5], to Hayabusa[6] to NEAR[7], authors have explored techniques based on optical systems or simple altimeter measurements for hovering, hopping, landing and station keeping[8–13]. Most of the work has been dedicated to the navigation of single spacecraft, though, more recently, interesting results have been presented on the possibility to navigate formations[14–17] or swarms of spacecraft[18].

Often optical navigation is used to determine the pointing direction to an object in the field of view after some image processing, such as the extraction of surface features or the contour of the lit surface [19]. Camera-based observations are, however, affected by range ambiguity. In some scenarios, like kinetic impactors, the knowledge of the range is less important [20] but it becomes essential if the spacecraft has to survive for a long time at a controlled distance from the surface of the minor body. This problem could be partially solved by using the known characteristics of the bodies in the field of view, such as their average diameter, but this technique cannot be directly used if the object has an irregular shape or the size is poorly known. Alternatively one can use a LiDAR or LRF to obtain more reliable range measurements to be used in combination with the pointing of the cameras [21] [16] [17]. Gil-Fernandez and Ortega-Hernando have demonstrated that a spacecraft can autonomously navigate around a binary asteroid system by observing only the primary at the cost of augmenting the estimated state with the estimation of the gravitational parameter of the asteroid and the pointing error due to the changing illumination conditions [22]. Stastny and Geller, instead, used optical observations of several of the moons of Jupiter to autonomously navigate a spacecraft around the giant planet [23].

This paper investigates the possibility to navigate in the proximity of a binary system by using optical navigation only. The navigation concept is similar to the one previously studied by Lasagni Manghi et al.[24] for the AIDA mission. In this paper, however, we consider the use of optical cameras operating in the visible range, we study the sensitivity to the knowledge of the orbital parameters of the secondary and we propose a state estimation process that simultaneously improves the knowledge of the motion of the secondary. The work in this paper extends previous studies by the authors on navigation in the proximity of single and binary asteroids [16, 17, 25, 26] and on asteroid deflection [27, 28]. The approach investigated in this paper uses the pointing vectors of the cameras to the primary and secondary asteroids in combination with the knowledge of the motion of the secondary asteroid around the primary to obtain an estimation of the position of the spacecraft with respect to the primary asteroid via a triangulation technique. It is shown that this triangulation method is highly sensitive to the knowledge of the motion of the secondary asteroid. The paper then proposes an augmented version of the triangulation method to allow for the inclusion of the estimation of the orbital elements of the secondary.

Four different scenarios are presented. The first represents the nominal case and is constituted by one spacecraft navigating around the equivalent L4 point of the system using the standard triangulation technique and perfect knowledge of the motion of the secondary asteroid. Then a sensitivity analysis is performed and the augmented triangulation

is introduced. A second scenario follows where the spacecraft also estimates the semi-major axis of the orbit of the secondary asteroid. The third scenario features the addition of a second spacecraft and the use of inter-spacecraft communication and relative position measurements. In the final scenario, the effect of the loss of the cameras on one of the spacecraft is assessed.

The paper is structured as follows. After the description of the dynamics and basic assumptions on the measurement model, the paper describes the basic triangulation technique followed by a brief presentation of the state estimation process. The analysis of the four scenarios follows with the description of the augmented measurement and state estimation technique for single and multiple spacecraft.

II. Dynamic Model

The dynamic environment in the proximity of binary asteroids is rich and complex due to their irregular shape and composition, the coupled interaction of their gravity fields, the third-body perturbation of the Sun and the effect of radiation pressure.

Since the main goal of this work is to test a navigation concept to control one or more spacecraft at a Lagrangian point of the binary system, we will consider a fictitious binary asteroid with simple but sufficiently rich dynamics that allow the illumination conditions of primary and secondary to be well defined. Thus the primary asteroid (asteroid A in the following) is modelled as a homogeneous sphere and the secondary (asteroid B in the following) as a homogeneous ellipsoid. This simplification still captures some key characteristics of binary systems like 1866 Sisyphus and 65803 Didymos and allows for the use of a simple monopole term for the gravity of the primary.

In addition to the gravitational pull of the primary and secondary asteroid, the third-body perturbation of the Sun is included together with the acceleration induced by the solar radiation pressure coming from the direct exposure of the spacecraft to sunlight. Other perturbations, such as the radiation pressure accelerations due to the albedo of the asteroids, are neglected. The reason for this is that the effects produced by these perturbations are smaller then the other effects.

The primary asteroid is assumed to move in the Ecliptic plane on a circular orbit and the orbit of the secondary with respect to the primary is also circular and contained in the Ecliptic plane. This simple model allows us to have repeatable eclipses of the secondary and of the spacecraft, which play a very important role in understanding if an optical navigation system in the visible range can be used. In addition, the secondary asteroid is a triaxial ellipsoid with semi-axes a_B , b_B and c_B and rotates around the z-axis with angular velocity ω_B [29], where the z-axis is perpendicular to the orbit plane and the rotation velocity is equal to the orbital angular velocity around the primary (i.e. the secondary is phase-locked).

The reference frame chosen for the simulation of the dynamics of spacecraft and asteroids is non-rotating and centred in the centre of mass of the binary system (see Fig. 1a). A body-fixed reference frame $\{O_B, \hat{X}_B, \hat{Y}_B, \hat{Z}_B\}$ centred in the centre of mass of the secondary asteroid is defined so that a_B is oriented along $\hat{X}_B$, b_B along $\hat{Y}_B$ and c_B along $\hat{Z}_B$. In

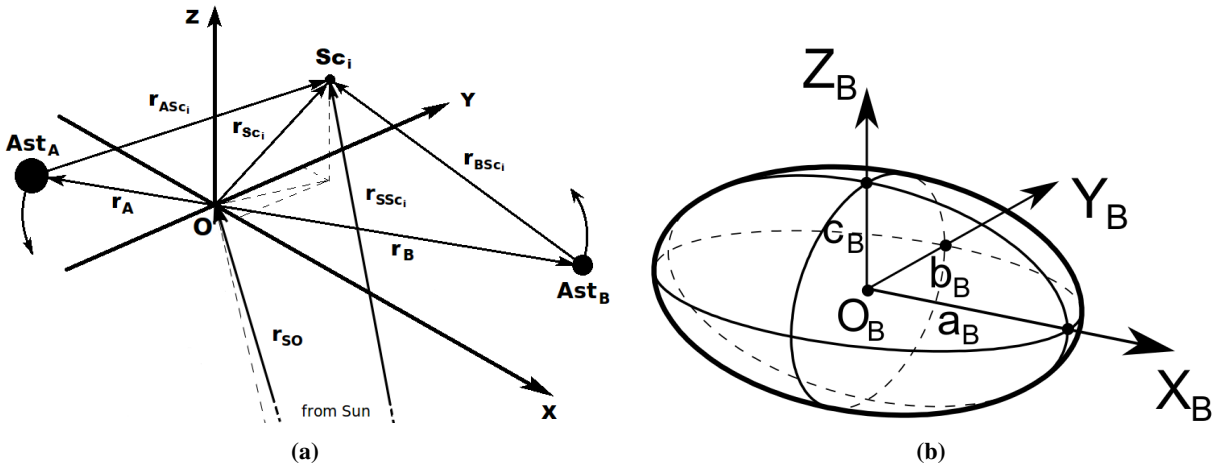

Fig. 1 Reference frames for the simulation dynamics: a) overall reference frame , b) body reference frame of Asteroid B.

this reference frame, the gravity field of the secondary asteroid can be expressed as the sum of a spherical field plus a second-degree and second-order field [30]:

$$ {}^{B}U_{20,22}\left(\theta_{Bi},\varphi_{Bi}\right)=\frac{\mu_B}{\|\delta\mathbf{r}_{BSc_i}\|^3}\left[{}^{B}C_{20}\left(1-\frac{3}{2}\cos^2(\theta_{Bi})\right)\quad+3{}^{B}C_{22}\cos^2(\theta_{Bi})\cos(2\varphi_{Bi})\right] \tag{1}$$

where $\delta\mathbf{r}_{BSc_i}$ is the relative position vector between the asteroid B and spacecraft i in the body-fixed frame B, μ_B is the asteroid gravitational parameter, the harmonic coefficients ${}^{B}C_{20}$ and ${}^{B}C_{22}$ are a function of the semi-axes:

$$ {}^{B}C_{20}=-\frac{1}{10}\left(2{c_B}^2-{a_B}^2-{b_B}^2\right);\quad {}^{B}C_{22}=\frac{1}{20}\left({a_B}^2-{b_B}^2\right) \tag{2}$$

and θ_{Bi} and φ_{Bi} are the latitude and longitude angles of spacecraft i in the body frame of B respectively:

$$ \theta_{Bi}=\tan^{-1}\left(\frac{z_{Bi}}{\sqrt{{x_{Bi}}^2+{y_{Bi}}^2}}\right);\quad \varphi_{Bi}=\tan^{-1}\left(\frac{y_{Bi}}{x_{Bi}}\right) \tag{3}$$

The conversion from the body-fixed frame to the reference frame is obtained by applying the rotation matrix:

$$ {}^{I}\mathbf{R}_B=\begin{bmatrix}\cos(\omega_B\,t) & -\sin(\omega_B\,t) & 0\\ \sin(\omega_B\,t) & \cos(\omega_B\,t) & 0\\ 0 & 0 & 1\end{bmatrix} \tag{4}$$

where t indicates the time. The spacecraft is assumed to be subject to the gravitational force of the Sun, solar radiation pressure and the irregular gravity of the binary system. With $\mathbf{r}_A$, $\mathbf{r}_B$, $\mathbf{r}_S$ and $\mathbf{r}_{Sc_i}$ as the position of asteroid A, asteroid B, the Sun and the i-th spacecraft respectively, it is possible to define $\mathbf{r}_{ASc_i}=\mathbf{r}_{Sc_i}-\mathbf{r}_A$, $\mathbf{r}_{BSc_i}=\mathbf{r}_{Sc_i}-\mathbf{r}_B$ and

$\mathbf{r}_{SSc_i} = \mathbf{r}_{Sc_i} - \mathbf{r}_S$ as the relative position vectors from the asteroids A and B and the Sun to the i-th spacecraft. From the definition of the reference frame and position vectors of the spacecraft, the non-linear equations of motion of the spacecraft can be written as:

$$\ddot{\mathbf{r}}_{Sc_i} = -\frac{\mu_A}{\|\mathbf{r}_{ASc_i}\|^3}\mathbf{r}_{ASc_i} - \left[\frac{\mu_B}{\|\mathbf{r}_{BSc_i}\|^3} + {}^{I}\mathbf{R}_B \frac{\partial^B U_{20,22}}{\partial \delta \mathbf{r}_{BSc_i}}\right]\mathbf{r}_{BSc_i} - \frac{\mu_S}{\|\mathbf{r}_{SSc_i}\|^3}\mathbf{r}_{SSc_i} + \frac{\mu_S}{\|\mathbf{r}_S\|^3}\mathbf{r}_S + \mathbf{a}_{SRP_i} + \mathbf{u_i} \tag{5}$$

with μ_S, μ_A and μ_B being gravity constants of the Sun, asteroid A and B respectively. The quantity $\mathbf{a}_{SRP_i}$ represents the acceleration induced by the solar radiation pressure on spacecraft i. Considering the spacecraft as a perfectly reflecting homogeneous sphere, $\mathbf{a}_{SRP_i}$ can be defined as:

$$\mathbf{a}_{SRP_i} = 2\, S_{SRP} \left(\frac{r_{1AU}}{r_{SSc_i}}\right)^2 \frac{A_i}{m_{Sc_i}} \frac{\mathbf{r}_{SSc_i}}{r_{SSc_i}} \tag{6}$$

where A_i and m_{Sc_i} are the spacecraft cross sectional area and mass respectively, S_{SRP} is the solar radiation pressure at 1 AU and r_{1AU} is the value of one astronomical unit in km. The vector $\mathbf{u}_i = [{}^x u_i, {}^y u_i, {}^z u_i]^T$ in equation (5) is a control input, which will be defined later in Section IV.A.

If one considers a formation of N spacecraft, the vector equation (5) can be applied to each spacecraft independently and can be re-written in compact form as a system of first order differential equations:

$$\dot{\mathbf{X}} = f_s\,(\mathbf{X}, \mathbf{u}) \tag{7}$$

where $\mathbf{X} = \left[\mathbf{r}_{Sc_1},\ \dot{\mathbf{r}}_{Sc_1},\ \mathbf{r}_{Sc_2},\ \dot{\mathbf{r}}_{Sc_2},\ \ldots, \mathbf{r}_{Sc_N},\ \dot{\mathbf{r}}_{Sc_N}\right]^T$ is the state vector containing the position and velocity of all the spacecraft, $\mathbf{u} = [\mathbf{u}_1,\ \mathbf{u}_2,\ \ldots \mathbf{u}_N]^T$ the vector containing all the control vectors and f_s is the right end side of Eq.(5) for all spacecraft.

A. Navigation dynamics

In order to introduce a degree of uncertainty in the actual location of the centre of mass of the binary system, the dynamical model used in the state estimation process is defined in a reference frame located in the expected centre of mass of asteroid A, that in all simulations in this paper is considered to be coincident with the geometric centre of the object. Given the difference in mass between the primary and the secondary, this change of reference frame introduces a small error in the dynamics that is modelled as process noise. Thus each spacecraft considers the modified dynamics:

$$\dot{\mathbf{x}} = f\,(\mathbf{x}, \mathbf{u}) \tag{8}$$

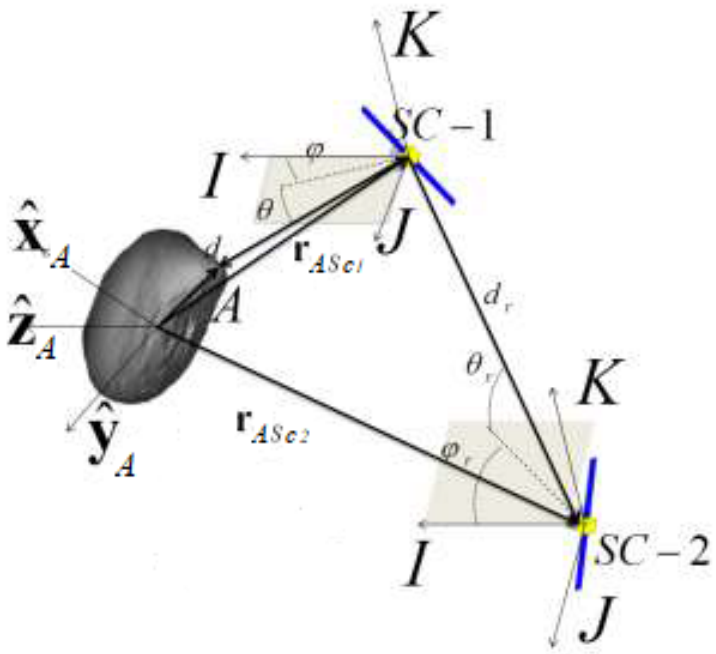

Fig. 2 Reference frame for the navigation dynamics.

in the estimation process, where $\mathbf{x} = [\mathbf{r}_{ASc_i}, \dot{\mathbf{r}}_{ASc_i}]^T$ is the state vector with respect to the centre of mass of asteroid A (see Fig. 1b.

III. Measurement Model

In this section we will describe the measurement models that are used in the simulations and the estimation process and the basic triangulation process at the basis of the navigation concept investigated in this paper. It is assumed that each spacecraft is provided with the following set of sensors:

- Two cameras, operating in the visible range of the spectrum and with finite resolution. The two cameras independently take images of the primary and secondary asteroids.
- One Sun sensor, used to determine the direction of the Sun.
- One inter-spacecraft relative state vector measurement unit that can measure the relative position vector.
- One star tracker that provides an estimation of the attitude of the spacecraft.

A. Camera Model

In order to develop the measurement model of the cameras, two intermediate reference frames are required as shown in Figure 3:

- Spacecraft coordinate system SC $\{x_{sc}\ y_{sc}\ z_{sc}\}$: the origin of this frame lies on the centre of mass of the spacecraft, with the coordinate axes coinciding with the three body axes[31] .

- Camera coordinate system C $\{\hat{x}_C\ \hat{y}_C\ \hat{z}_C\}$: the centre C is the perspective projection of the camera, with the z_C-axis parallel to the optical axis of the camera and directed to the centre of the targeted asteroid. The image plane is defined as O_C-x_C y_C.

In this paper, it is assumed that the body reference frame of each spacecraft is aligned with the principal inertial frame of the spacecraft and the attitude is known with a level of precision corresponding to that provided by a good star tracker.

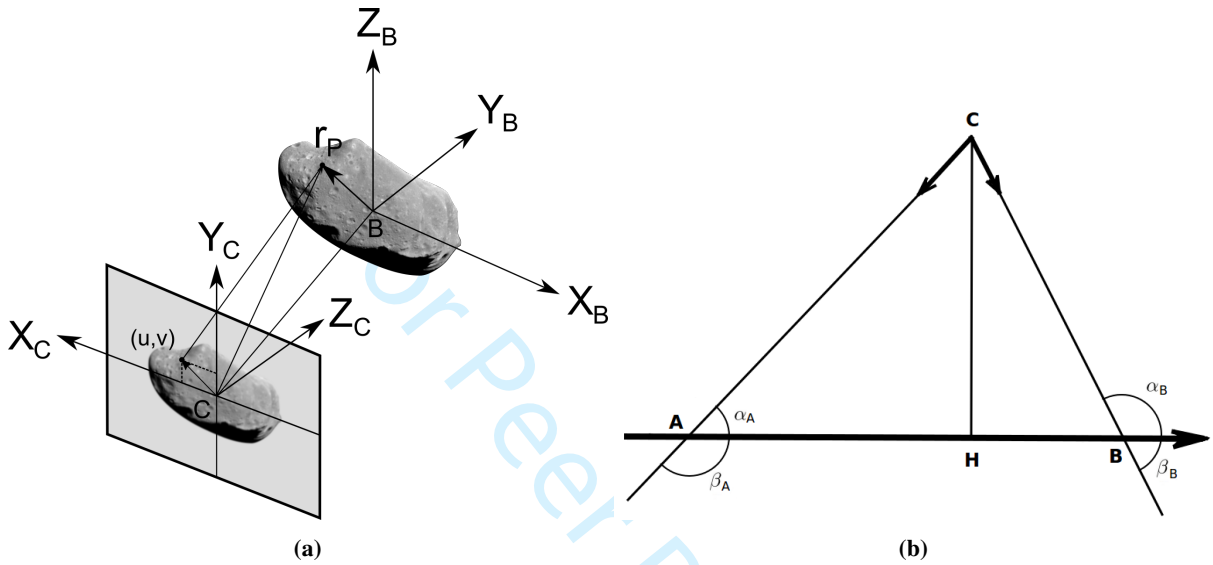

Fig. 3 Camera and basic triangulation models: a) projection of asteroid B on the image plane of the camera; b) basic triangulation scheme.

The picture generation algorithm is composed of different stages, outlined in Algorithm 1. The first stage (line 1 in Algorithm 1) is a simple re-orientation of the spacecraft to point the cameras to the expected centroid of the objects in view. At time t_0 the direction of the centroid is given by the previous knowledge on the asteroid, while at subsequent times it comes from the previous estimation of the relative state vector. Note that since the spacecraft is at L4 and maintain its position with respect to L4, only one object can be in view of each camera. In the second stage (line 2 of Algorithm 1) we add some random noise ζ_{AOCS} to the pointing of the cameras. Stage 3 (line 3 of Algorithm 1) projects the image on the image plane of the camera. Using the information from the Sun sensor, stage 4 (line 4 of Algorithm 1) rotates the image so that the Sun is always on the left side of the image. This is not a strictly necessary step but it facilitates the identification of the limb in Algorithm 2. A noise on the identification of the direction of the Sun is then added to the orientation of the image. Finally we render the image on the image plane considering the actual number of pixels, aperture and focal length. The software used to render the image is an open source code available on Github (github.com/Steve132/uraster). Note that the pixelisation error is introduced at this stage, with the transformation of the information from a continuous domain to a discretised one. Its effects depend on the number of pixels used and the field

of view of the camera (see Section V for the specifications of the camera).

Algorithm 1 : Image Generation

1: Point camera to target
2: Add pointing accuracy noise ζ_{AOCS}
3: Projection onto the image plane
4: Rotate camera image
5: Add Sun direction noise ζ_{SS}
6: Render image

B. Image Processing and Limb-fitting Algorithm

Once a new image is generated (Figure 4, top left), an image processing algorithm is used to compute the pointing vector to the centroid of the object in the image plane (see Algorithm 2 and Fig.4). The first step (line 1 of Algorithm 1) is to apply an intensity filter that sets all pixels with a light intensity below a given threshold to 0. After that (line 2 of Algorithm 1) a scanning loop identifies the illuminated edge of the object before a limb fitting algorithm[19] is applied (line 3 of Algorithm 1)) and the position of the centroid calculated (line 4 [19]).

Algorithm 2 : Limb Fitting and Centroiding

1: Image filtering (see Fig. 4b)
2: Object edge identification (see 4c)
3: Limb fitting
4: Centroiding (see 4d)

Once the location of the centroid is known, the pointing vector can be computed as:

$$\mathbf{V}_{ij} = \left[{}^{C}x_{ij},\ {}^{C}y_{ij},\ f_C\right]^T \tag{9}$$

where the C stands for *camera*, f_C is the focal length of the camera, the subscript i identifies the i-th spacecraft and j the j-th target. Finally, the pointing vector is normalised and rotated back to the principal reference frame, generating the measurement vector:

$${}^{P}\mathbf{y}_{ij} = {}^{I}\mathbf{R}_{SC_i} \cdot {}^{SC_i}\mathbf{R}_{C_i} \cdot \mathbf{V}_{ij} = \left[{}^{P}x_{ij},\ {}^{P}y_{ij},\ {}^{P}z_{ij}\right]^T \tag{10}$$

where ${}^{SC_i}\mathbf{R}_{C_i}$ is the rotation matrix from camera to body frame for spacecraft i, ${}^{I}\mathbf{R}_{SC_i}$ the rotation matrix from the body frame of spacecraft i to inertial frame and the superscript P stands for *pointing*.

Figure 5 shows the output of the ellipse fitting algorithm at different times with different illumination conditions for both of the asteroids. In those images, the blue contour is the ellipse, with its centre marked with a star. Then the red diamond represents the real centre of mass of the target object as seen on the camera plane while the green diamond is the centre of the image. In general we would expect that the centre of the object would not coincide with the centre of

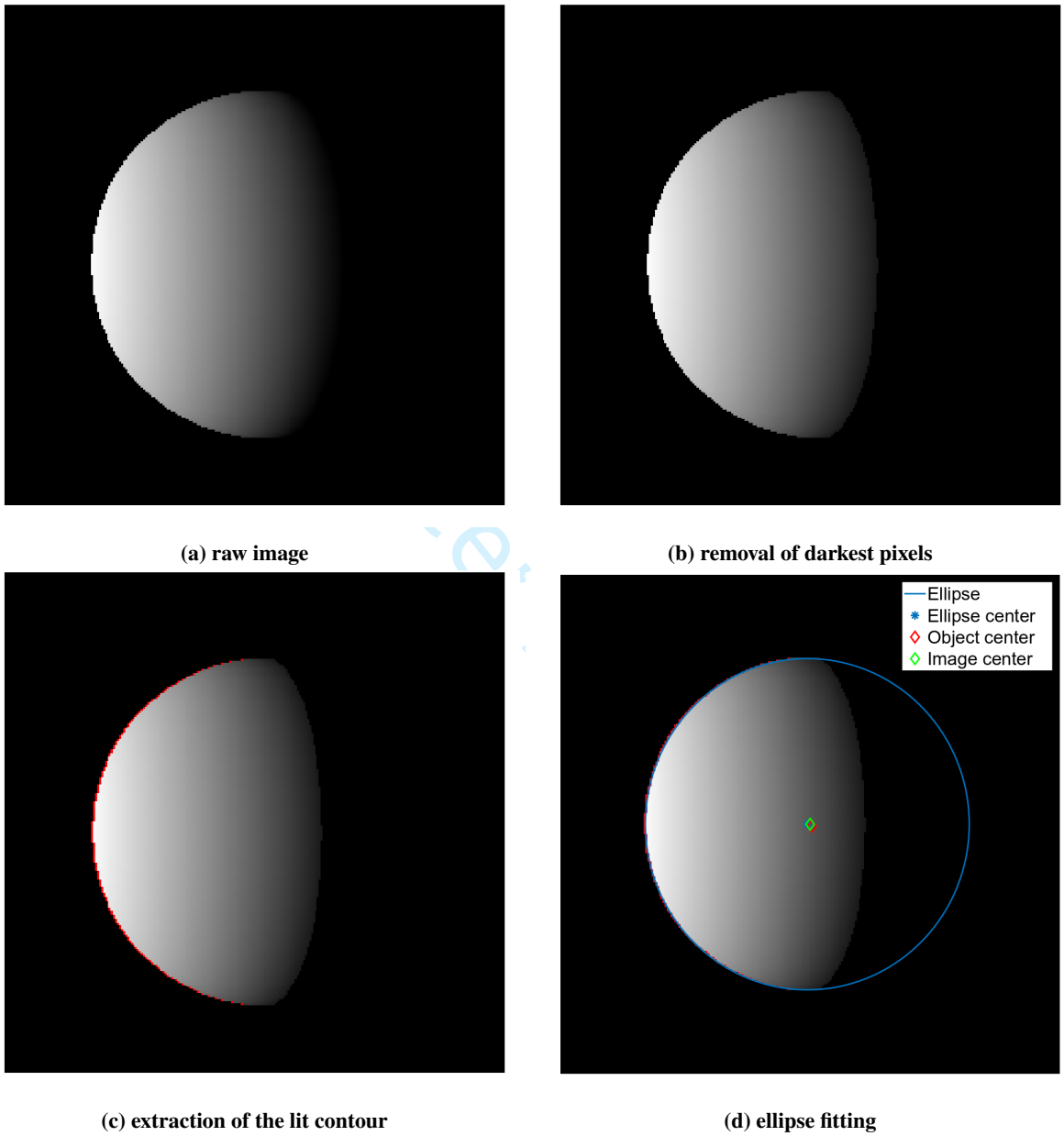

(a) raw image

(b) removal of darkest pixels

(c) extraction of the lit contour

(d) ellipse fitting

Fig. 4 Camera and basic triangulation models: a) projection of asteroid B on the image plane of the camera; b) basic triangulation scheme.

the image because of the pointing errors of the camera. Instead, the best result would be to have the centre of the ellipse coincide with the centre of the object. This works well in the case of the spherical object, with the two points being close together even under poor illumination conditions where a small portion of the object is illuminated. However, the performance degrades in the case of the ellipsoidal asteroid. When most of an ellipsoid's surface is illuminated, the algorithm manages to determine the centroid quite well, but when only a small portion is illuminated, instead, the error of the position of the centroid increases.

This is a limitation of the centroid determination algorithm as the pointing vectors to the centroids of the asteroid will be affected by larger errors under the poor illumination conditions at *dawn* and *sunset*. These effects can be mitigated by increasing the resolution of the cameras and reducing their field of view. Furthermore, we introduced a lower limit of 50 illuminated pixels for the image to be processed to avoid calculating the centroid with limited information.

C. Basic Triangulation Method

Once the two pointing vectors and the relative position vector are available, the resulting geometry consists of a triangle. According to Fig. 3b the spacecraft will occupy the vertex C, while the vertices A and B will be occupied by the two asteroids. The segment $\mathbf{r}_{AB}$ identifies the relative position vector between the two asteroids. The angles β_{iA} and β_{iB} are defined as:

$$\beta_{iA} = acos\left(\frac{\mathbf{r}_{AB} \cdot {}^{P}\mathbf{y}_{iA}}{\|\mathbf{r}_{AB}\|}\right); \qquad \beta_{iB} = acos\left(\frac{\mathbf{r}_{AB} \cdot {}^{P}\mathbf{y}_{iB}}{\|\mathbf{r}_{AB}\|}\right) \tag{11}$$

that yield $\alpha_{iA} = \pi - \beta_{iA}$ and $\alpha_{iB} = \pi - \beta_{iB}$. Once the angles α_{iA} and α_{iB} and the length of the segment $\mathbf{r}_{AB}$ are known, the triangle is fully determined. The length of the segment $\mathbf{r}_{AC_i}$ can be obtained from:

$$\|\mathbf{r}_{AC_i}\| = \frac{sin(\alpha_{iB})}{sin(\alpha_{iB} - \alpha_{iA})}\|\mathbf{r}_{AB}\| \tag{12}$$

Multiplying the value of $\|\mathbf{r}_{AC_i}\|$ by the respective pointing vector, ${}^{P}\mathbf{y}_{iA}$, provides the relative position vector between the spacecraft at C and the asteroid A. Given that, in the reference frame of the navigation dynamics, asteroid A is placed at the origin, the opposite of the relative position vector represents the absolute position vector of the spacecraft in that reference frame:

$${}^{T}\mathbf{y}_i = -\|\mathbf{r}_{AC_i}\| \cdot {}^{P}\mathbf{y}_{iA} \tag{13}$$

It is important to note that Eq. (12) is undetermined when the triangle degenerates. This happens in two cases: when the three vertices are aligned and when $\mathbf{r}_{AC_i}$ and $\mathbf{r}_{BC_i}$ are parallel (C at infinity). In the former case, both α_{iA} and α_{iB} are equal to zero or π and the ratio of the two sine functions will be undetermined; in the latter case, $\alpha_{iA} = \alpha_{iB}$,

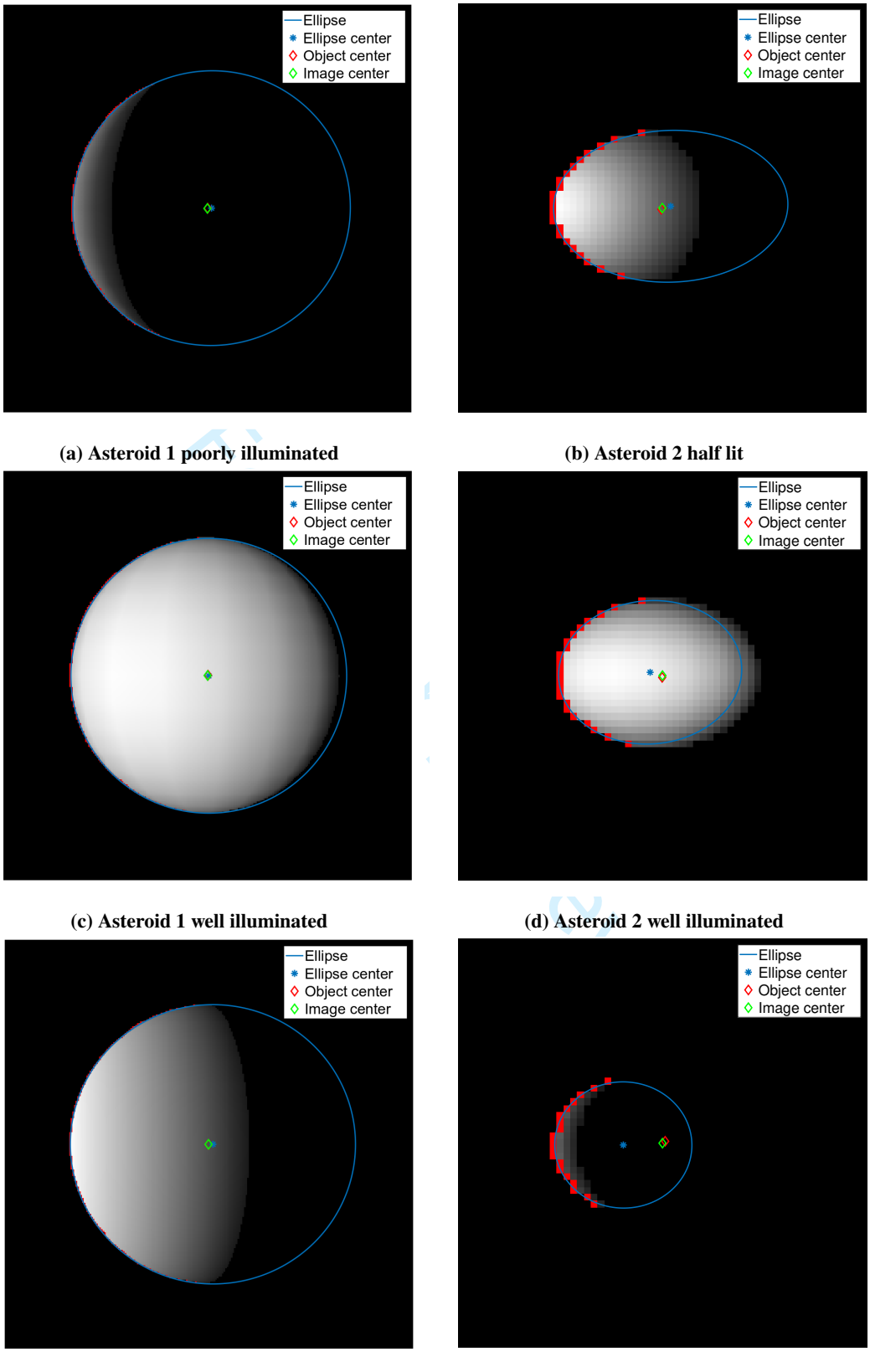

(a) Asteroid 1 poorly illuminated

(b) Asteroid 2 half lit

(c) Asteroid 1 well illuminated

(d) Asteroid 2 well illuminated

(e) Asteroid 1 half lit

(f) Asteroid 2 poorly illuminated

Fig. 5 Performances of the ellipse fitting algorithm for different illumination conditions.

then the denominator is equal to zero, making the ratio tend to infinity.

It is crucial to understand how dependent this method is on the knowledge of the motion of the secondary asteroid with respect to the primary. In fact, the relative position vector between them, $\mathbf{r}_{AB}$ contributes, in equation (12), to all the terms involved, given that also α_{iA} and α_{iB} are obtained from its orientation. The effects of an imperfect knowledge of the motion of the secondary asteroid will be investigated in Section V.A.

D. Inter-spacecraft Measurements

The inter-spacecraft metrology system is inspired to the system already flight tested on the PRISMA mission [32]. In [32] the authors propose a metrology system that provides both line of sight and range with very simple low cost radio-metric measurement using multiple receiving antennas. A similar metrology system based on difference in Time Of Arrival and Frequency Of Arrival was also demonstrated in [33]. The inter-spacecraft measurement consists of the relative position vector between the two spacecraft in the formation, expressed in the principal reference frame. When a new measurement needs to be computed, the initial relative position vector is composed of the relative distance, local azimuth and elevation, computed in the reference frame of the sensor [34]. The observation equation is given by:

$$\rho_{ij} = h_r\left(\mathbf{r}_{Sc_i},\ \mathbf{r}_{Sc_j}\right) = [d_r\ \varphi_r\ \psi_r]^T + \zeta_r \tag{14}$$

where $\zeta_r = \left[\zeta_{d_r}\ \zeta_{\varphi_r}\ \zeta_{\psi_r}\right]^T$ is the measurement noise. The vector is then converted into a Cartesian expression and transformed in to the principal reference frame:

$${}^{R}\mathbf{y}_{ij} = \begin{bmatrix} (d_r + \zeta_{d_r})\ cos(\psi_r + \zeta_{\psi_r})\ cos(\varphi_r + \zeta_{\varphi_r}) \\ (d_r + \zeta_{d_r})\ cos(\psi_r + \zeta_{\psi_r})\ sin(\varphi_r + \zeta_{\varphi_r}) \\ (d_r + \zeta_{d_r})\ sin(\psi_r + \zeta_{\psi_r}) \end{bmatrix} \tag{15}$$

It is important to note that this measurement depends on the knowledge of the positions of the two spacecraft. When a new measurement is simulated, these positions are known exactly; on the other hand, when simulating the measurement during the estimation process, this information needs to be available to each spacecraft. While each spacecraft knows its own state due to the estimation process, the knowledge of the state of another member of the formation is generally unknown. There are two possible solutions: the first one is that each spacecraft estimates the states of all the members of the formation; the second one requires each spacecraft to transmit the estimation of its own state. The first method places significant computational demands on each spacecraft whereas using the second approach makes the simulated measurement depend on the *reliability* of the information provided by the other spacecraft. In this paper the latter method is chosen.

IV. State Estimation and Control

The state estimation process is based on the same Unscented H_∞ Filter (UHF) proposed in [11, 16] and [17]. The use of an unscented filter is motivated by the expectation that the dynamics of the spacecraft could be significantly non-linear, furthermore given the potentially significant uncertainty in the measurements, it is desirable to have some level of robustness in the filtering process. In previous work [16] ran a comparative analysis of different filters on a similar problem and the UHF resulted to be a good compromise between robustness and computational complexity. For this reason, in this work we directly start with the filter selected in [16].

The UHF works on the premise that one can find a good approximation for the *a posteriori* covariance by propagating a limited set of optimally chosen samples [35]. Using the estimation theory formalism, the non-linear process in Eq. (7) and the measurement equations can be discretised in time and written as:

$$\begin{aligned} \mathbf{x}_{k+1} &= f\left(\mathbf{x}_k,\ \mathbf{u}_k\right) \\ \mathbf{y}_k &= h\left(\mathbf{x}_k,\ \mathbf{v}_k\right) \end{aligned} \tag{16}$$

where $\mathbf{v}_k$ is the measurement noise and $\mathbf{u}_k$ is the control, that will be discussed later in Section IV.A. In general, the observations will assume the structure:

$$\mathbf{y}_k = \left[{}^{T}\mathbf{y}_{i_k},\ {}^{R}\mathbf{y}_{ij_k}\right]^T \tag{17}$$

The initial conditions are the estimated position and velocity as computed by the filter at time t_k. The UHF relies on the unscented transformation to propagate a set of suitable sigma points, drawn from the *a priori* covariance matrix. The set of sigma points χ is given as:

$$\chi_k^i = \begin{cases} \tilde{\mathbf{x}}_k & i = 0 \\ \tilde{\mathbf{x}}_k + \left(\sqrt{\left(n + k_{UHF}\right)\mathbf{P}_k}\right)_i & i = 1,\ 2,\ \ldots,\ n \\ \tilde{\mathbf{x}}_k - \left(\sqrt{\left(n + k_{UHF}\right)\mathbf{P}_k}\right)_i & i = n+1,\ \ldots,\ 2n \end{cases} \tag{18}$$

where χ is a matrix consisting of (2n+1) column vectors, each one representing the last estimated state augmented by some error dependent on the last associated covariance matrix. k_{UHF} is a scaling parameter that in this work is set equal to 10^{-2}. The sigma points are transformed or propagated through the non-linear function, the so-called unscented transformation. Once the sigma points are propagated until time t_k, they are used to compute the mean of the predicted state vectors $\hat{\mathbf{x}}_{k|k-1}$ and the mean observation $\hat{\mathbf{y}}_{k|k-1}$ as:

$$\begin{aligned}
\chi^i_{k|k-1} &= f\left(\chi^i_{k-1},\ \mathbf{u}_{k-1}\right) \\
\hat{\mathbf{x}}_{k|k-1} &= \sum_{i=0}^{2n} W_i\ \chi^i_{k|k-1} \\
\hat{\mathbf{y}}_{k|k-1} &= \sum_{i=0}^{2n} W_i\ h\left(\chi^i_{k|k-1}\right)
\end{aligned} \tag{19}$$

where $\mathbf{W}$ is a vector of weights defined as:

$$\begin{aligned}
W_0 &= k_{UHF}/(n + k_{UHF}) \\
W_i &= k_{UHF}/[2(n + k_{UHF})], \quad i = 1,\ 2,\ \ldots,\ 2n
\end{aligned} \tag{20}$$

The associated predicted state covariance matrix $\mathbf{P}_{k|k-1}$, the predicted measurement covariance matrix $\mathbf{P}^{yy}_{k|k-1}$ and the cross correlation covariance matrix $\mathbf{P}^{xy}_{k|k-1}$ can be computed as:

$$\begin{aligned}
\mathbf{P}_{k|k-1} &= \sum_{i=0}^{2n} W_i \left[\chi^{\mathbf{i}}_{\mathbf{k}|\mathbf{k-1}} - \tilde{\mathbf{x}}^-_k\right]\left[\chi^{\mathbf{i}}_{\mathbf{k}|\mathbf{k-1}} - \tilde{\mathbf{x}}_{k|k-1}\right]^T + \mathbf{Q} \\
\mathbf{P}^{yy}_{k|k-1} &= \sum_{i=0}^{2n} W_i \left[h\left(\chi^i_{k|k-1}\right) - \tilde{\mathbf{y}}^-_k\right]\left[h\left(\chi^i_{k|k-1}\right) - \tilde{\mathbf{y}}^-_k\right]^T + \mathbf{R} \\
\mathbf{P}^{xy}_{k|k-1} &= \sum_{i=0}^{2n} W_i \left[\chi^{\mathbf{i}}_{\mathbf{k}|\mathbf{k-1}} - \tilde{\mathbf{x}}^-_k\right]\left[h\left(\chi^i_{k|k-1}\right) - \tilde{\mathbf{y}}^-_k\right]^T
\end{aligned} \tag{21}$$

where $\mathbf{Q}$ is the weight matrix associated to the navigation dynamics and $\mathbf{R}$ the one associated to the measurements. These matrices are used to give more or less importance to either the prediction or the measurements Finally, the new estimated state vector $\tilde{\mathbf{x}}_k$ and the corresponding covariance matrix $\mathbf{P}_{x,k}$ can be computed as:

$$\begin{aligned}
\tilde{\mathbf{x}}_k &= \hat{\mathbf{x}}_{k|k-1} + \mathbf{P}^{xy}_{k|k-1}\left(\mathbf{P}^{yy}_{k|k-1}\right)^{-1}(\mathbf{y}_k - \tilde{\mathbf{y}}_k) \\
\mathbf{P}_k &= \mathbf{P}_{k|k-1} - \left[\mathbf{P}^{xy}_{k|k-1}\ \mathbf{P}_{k|k-1}\right] R^{-1}_{e,k}\left[\mathbf{P}^{xy}_{k|k-1}\ \mathbf{P}_{k|k-1}\right]^T
\end{aligned} \tag{22}$$

where

$$R_{e,k} = \begin{bmatrix} \mathbf{P}^{yy}_{k|k-1} & \left[\mathbf{P}^{xy}_{k|k-1}\right]^T \\ \mathbf{P}^{xy}_{k|k-1} & \mathbf{P}_{k|k-1} - \gamma^2\mathbf{I} \end{bmatrix}; \qquad \gamma^2 = \alpha_{UHF}\, max\left(eig\left(\mathbf{P}^{-1}_{k|k-1} + \mathbf{P}^{-1}_{k|k-1}\mathbf{P}^{xy}_{k|k-1}\mathbf{R}^{-1}\left[\mathbf{P}^{-1}_{k|k-1}\mathbf{P}^{xy}_{k|k-1}\right]^T\right)^{-1}\right) \tag{23}$$

The value of the parameter γ^2 is crucial to guarantee the positiveness of $\mathbf{P}_k$ and hence the existence of the H_∞ filter. The parameter α_{UHF} must be a scalar larger than one and throughout this work it is set equal to 2.

From the set of equations (22), the performance bound γ^2 has no direct effect on the calculation of the estimated state.

Nonetheless γ^2 modifies the shape of the covariance matrix update, which, in turn, generates a different distribution of the sigma points. In this way, the propagation and the update step at the following time step will be directly influenced by the value of the performance bound.

A. Control Strategy

Although the scope of the paper is not to develop a control strategy, the implementation and testing of the navigation algorithms still required to maintain the spacecraft at L4. Thus, the control strategy proposed in this section aims at keeping each spacecraft near L4. The controller is based on a proportional–derivative (PD) control law:

$$\mathbf{u} = K_P \left([x, y, z]_G^T - [x, y, z]_N^T \right) + K_D \left([\dot{x}, \dot{y}, \dot{z}]_G^T - [\dot{x}, \dot{y}, \dot{z}]_N^T \right) \tag{24}$$

where the subscript G indicates the estimated coordinates and velocity of L4 and the subscript N indicates the estimated position and velocity of the spacecraft. The parameter K_P is the proportional coefficient and K_D is the derivative coefficient. Control (24) is introduced into the full dynamic model in Eq. (5). The two weights K_P and K_D were tuned, over several simulations, to get an acceptable response with a low control acceleration. The values of the weights and the control response can be found in section V. Note that, the controller continues acting on the spacecraft at any time, including the eclipse phases. Furthermore, in the event in which the dynamical characteristics of the binary are not known exactly the position and velocity of L4 are only estimated as part of the filtering process.

V. Navigation Analysis

The binary asteroid system chosen as an environment for the simulations is 65803 Didymos, whose parameters are listed in Table 1 [36]. The duration of the simulations is set to 10.4 times the orbital period of the secondary asteroid around the primary, T_{AB}, equal to approximately 124 hours. For simplicity reasons, the orbital motion of the system around the Sun has been considered circular; the rotation of the secondary asteroid around the first is assumed on the same plane of the motion of the binary around the Sun. The dimensions, gravitational parameters and angular velocities are chosen according to the current knowledge of the system, with the secondary asteroid being tidally locked with respect to the first one.

For the first navigation analysis, one single spacecraft was placed in the proximity of the L4 Lagrangian point of the binary asteroid system. The spacecraft is equipped with two cameras with a field of view of 90 deg and capable of generating 500x500 pixels images. It is assumed that the AOCS guarantees a pointing accuracy with standard deviation of 10^{-3} rad and new pictures are generated every 5 minutes. From geometrical considerations, using Equations (11), (12) and (13), an error or 10^{-3} rad in the in-plane pointing of both the cameras, at the L4 position for this system (asteroids A and B are 1.2 km apart), would produce a measurement error of about 2.4 m on the y-axis. In addition

Table 1 Orbital and physical parameters for 65803 Didymos

Semi-major axis	a	1.6446 AU
Eccentricity	e	0.3838
Inclination	i	3.4077 deg
RAAN	Ω	73.2219 deg
Argument of periapsis	ω	319.2516 deg
Orbital period	T_D	2.11 yr
Distance AB	d_{AB}	1.18 km
System rot. period	T_{AB}	11.92 h
Grav. param. A	μ_A	$3.4908 * 10^{-8} km^3/s^2$
Physical dimensions	a_A, b_A, c_A	387.5, 387.5, 387.5 m
Rotational period	T_A	2.26 h
Grav. param. B	μ_B	$3.1781 * 10^{-10} km^3/s^2$
Physical dimensions	a_B, b_B, c_B	81.5, 62.7, 52.2 m
Rotational period	T_B	11.92 h

to the AOCS error, the pixelisation also contributes to the pointing uncertainty. If the centroiding process produces an error of 1 pixel, at the centre of the camera's field of view, where the effect is maximised, the respective angular error would be 4×10^{-3} rad. This alone would produce a position error of 9.7 m. This would also decrease if the spacecraft gets closer to the asteroids and would increase if it gets further away. Given the absence of measurements for long periods of time due to eclipses, causing the spacecraft to drift away from L4, the low accuracy of the centroiding process at the beginning and end of eclipses, a value of 20 m has been chosen as the average maximum expected error on the position components coming from Equation (13). This leads to the choice of the weight matrix R, associated to the measurements (Eq. (13)) as a 3x3 diagonal matrix with values equal to $4 \times 10^{-4} km^2$. Regarding the navigation dynamics, this differs from the simulation dynamics only because of the absence of the non-inertial accelerations arising from the shift of the origin from the centre of mass of the binary system to the centre of mass of the primary asteroid. Such accelerations are very small, because of the relatively small mass of the binary system and the small amplitude of the motion of the primary asteroid around the centre of mass of the system, that actually lies inside the primary asteroid. Hence its associated weight matrix, **Q**, is a set as a 6x6 diagonal matrix with the first three elements equal to $10^{-12} km^2$ and the last three equal to $10^{-12} km^2/s^2$.

The controller starts working after 2 hours to give time to the filter to reduce the estimation error. The area to mass ratio of the spacecraft, at start of operations, is 0.04 m^2/kg and the spacecraft is assumed to be perfectly reflective. The initial estimated state has an error in each component of the state vector that is equal to 20% of the nominal value (the exact state of L4 in the binary system). A set of 100 simulations was run and the mean of the error in position and velocity, together with their respective 1-σ uncertainty, was computed at every instant of time for the duration of the whole simulation.

To fully understand the results it is necessary to consider the real and estimated trajectories and the estimation errors at the same time. Figure 6 shows two different representations of the real and estimated trajectories of the spacecraft around the Lagrangian point for a single run: the first one is depicted in the principal reference frame; the second one in a reference frame centred on the main asteroid and rotating with the binary system.

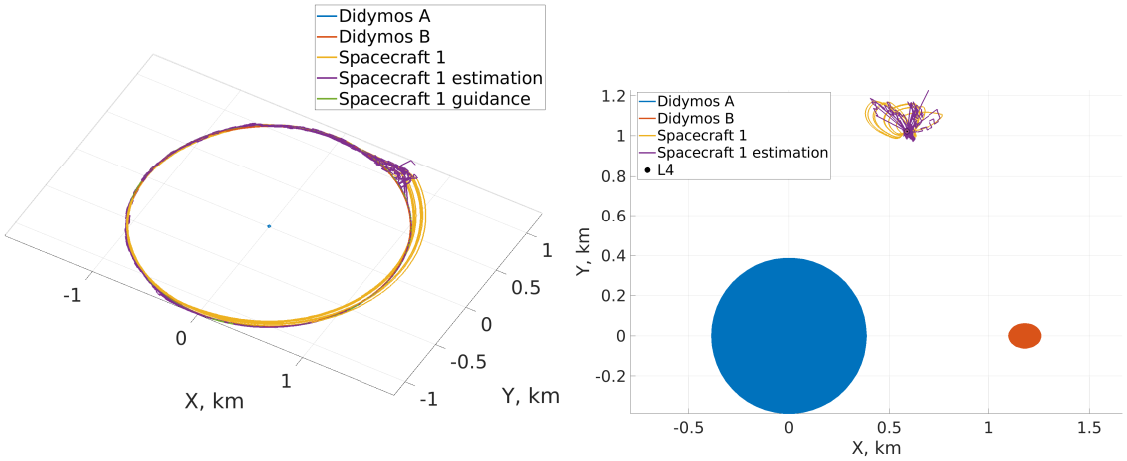

(a) Non-rotating frame **(b) Rotating frame**

Fig. 6 Real and estimated trajectory of the spacecraft in the non-rotating frame and in a frame rotating with the asteroids.

Figure 7 gives a position components breakdown of the estimation results. It is composed as follows:

- the black solid lines represent the mean estimation error across the 100 runs, computed as the position of the spacecraft estimated by the filter minus the truth state, at each time step.
- the black dashed lines represent the $\pm 1\sigma$ dispersion of the results of the 100 runs around the mean.
- the red solid lines represent the mean value across the 100 runs of the $+1\sigma$ uncertainty on the estimated state provided by the filter at each time step.
- the red dashed lines represent the respective $\pm 1\sigma$ dispersion of the values of the 100 runs.
- the blue solid lines represent the mean value across the 100 runs of the -1σ uncertainty on the estimated state provided by the filter at each time step.
- the blue dashed lines represent the respective $\pm 1\sigma$ dispersion of the values of the 100 runs.

It can be seen that, for each component, the mean values, black lines, indeed oscillate around 0 and that, as long as new measurements are provided, they stay within the $\pm 1\sigma$ estimate envelope, red and blue lines. Another useful information is that the 1σ dispersion of the estimated 1σ uncertainty, red and blue dashed lines, is very small, hence their 3σ envelopes would not be very different. Also, given the amplitude of the 1σ dispersion of the estimated position error, black dashed lines, it is safe to state that its 3σ envelope is also contained within the red and blue lines.

For the sake of simplicity, rather than displaying the single estimation error components, their norm is preferred. This

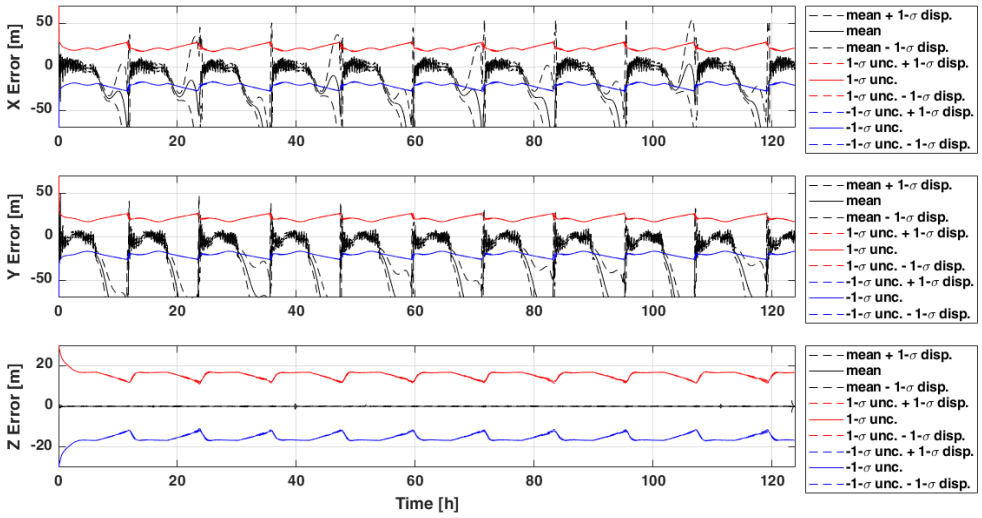

Fig. 7 Position estimation error components and respective 1-σ uncertainty

means that, for each time step the estimation error (estimated position minus truth state) is computed first and then its norm. This reduces the variables to display from 3 to 1 at the expense of a loss of information. Indeed, with the three components visualisation the amount of error on each direction is known. With the norm, instead, it can only be said that the truth state is at a certain distance from the estimated one. It is important to say that this is just a visualisation choice and that the filter always estimates and uses all the state components. The result of this stylistic choice can be seen in Figure 8. Here the blue lines represent the mean value, over 100 runs, of the estimation error, thus being the norm equivalent of the black solid lines of the component figure, while the red lines represent the mean value of its 1σ uncertainty as estimated by the filter, thus equivalent to the red and blue solid lines of the component figure. For the same reason as before, the respective 1σ distributions are neglected. Given that the blue lines display the norm of the position error components, they can never have negative values and then displaying only the upper side of the 1σ uncertainty is enough.

Figure 8, instead, shows the estimation errors on both position and velocity, together with their 1-σ uncertainty. Analysing the evolution of the estimation errors, it can be seen that a noisy period is always followed by a relatively smooth one where the error increases. This smooth period occurs because of the lack of acceptable optical images of both asteroids and is characterised by the absence of measurements. In order to have a measurement, in fact, the illumination conditions of the two bodies must guarantee a number of illuminated pixels high enough to extract the contour of the object and fit the ellipse for the computation of the centroid. Given that the motion of the Sun is on the same plane of the motion of the two asteroids around the centre of mass of the binary system, for roughly half of the system period (6 hours) the spacecraft cannot see both asteroids with a sufficient number of illuminated pixels. We call these periods eclipse periods. In this case, the position and velocity errors shown are computed according to the

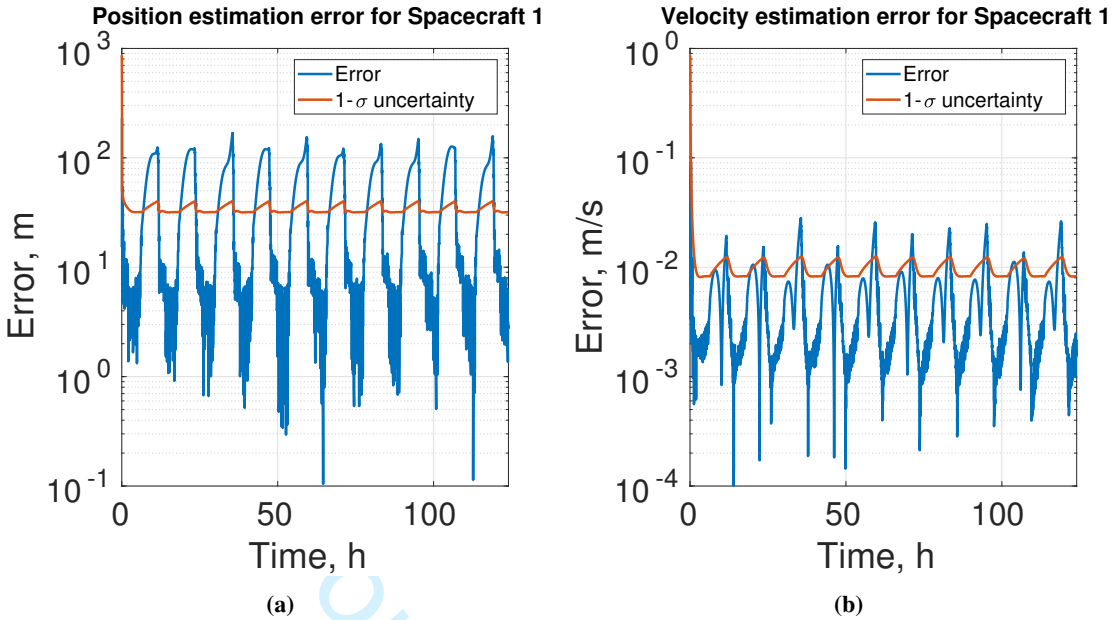

Fig. 8 Mean values of the estimated position and velocity errors and respective 1-σ uncertainty for the nominal case: a) error in position and b) in velocity.

navigation state obtained through the propagation of the last estimated state by the navigation dynamics. Under these conditions, in fact, the controller acts according to the comparison between the guidance and the state propagated by the navigation dynamics. Due to the finite error at the beginning of the propagation, the propagated state starts diverging from the real one.

On the other hand, the control is still computed and acts on the spacecraft. The result is quite interesting. A closer look at the trajectories show that the navigation and guidance trajectories follow the same path, although with some noise. However, the controller leads the spacecraft on a different trajectory. Only when new measurements are available again the spacecraft realises that it is off-course and corrects its path. In Figure 8, the average position error is stable at about 10 m due to the limited excursions of the spacecraft. Nevertheless, it can be seen that bigger variations in the position error occur at the beginning and end of each eclipse phase. This can be easily attributed again to the poor illumination conditions typical of these phases, as previously shown in Figure 5.

One might consider to switch off the controller during the eclipses and let the spacecraft follow the natural dynamics. However, the related simulations showed that the spacecraft would experience greater diversions, in some cases going inside the nominal trajectory and getting very close to a collision with the asteroids. Fig. 9 shows the control acceleration profile for the case analyzed in this section. The peak acceleration remains contained and is consistent with an ion engine, leading to only a few grams of propellant if one assumes a specific impulse of 4500s.

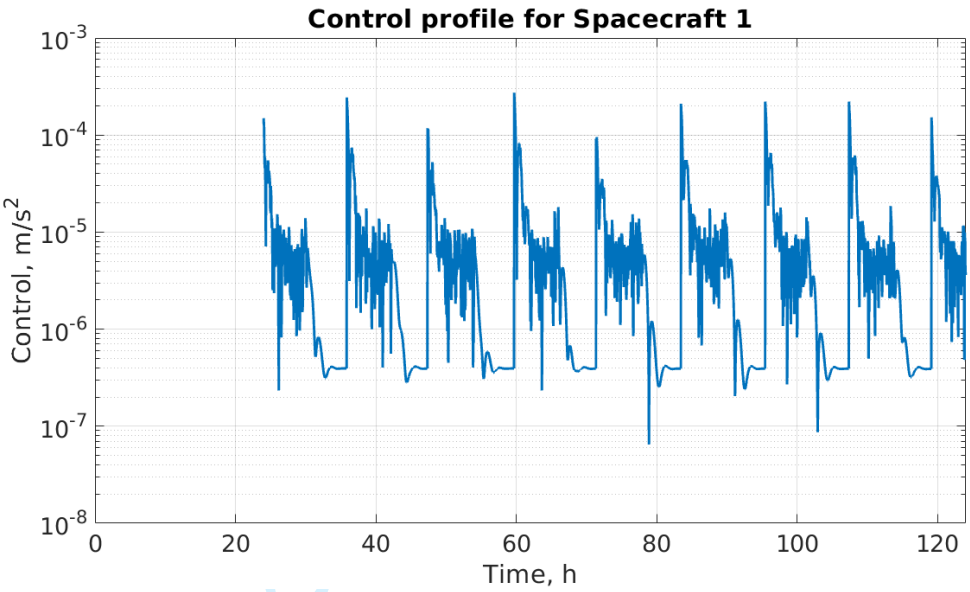

Fig. 9 Control acceleration for the nominal case.

A. Sensitivity analysis

As stated in Section III.C, the efficacy of the triangulation model depends on the knowledge of the motion of the secondary asteroid around the primary. In a previous work [26] it was shown how inaccuracies on the knowledge of the inclination or the initial true anomaly of the asteroid can lead to large errors in the state estimation of the spacecraft.

A sensitivity analysis is now presented to assess how the error on different orbital parameters affect the state estimation of the spacecraft. The parameters chosen for the analysis are the semi-major axis (SMA), the eccentricity (ECC) and the inclination (INC) of the orbit (see Table 2 where the errors on the nominal values, or Δ's, are in brackets).

1. Single parameter analysis

A first analysis was performed varying one parameter at the time and using the expected error on the estimation of the orbital parameters as reported in reference [36]. These values are listed in Table 2.

Table 2 Reference values and uncertainty on the orbital parameters of the secondary asteroid

SMA, km	Δ SMA	ECC	Δ ECC	INC, deg	Δ INC
1.18	(+0.04)	0.0	(+0.03)	0.0	(+25.0)
	(- 0.02)		(- 0.0)		(- 0.0)

For each value of the orbital parameters 100 simulations were run and the mean on the error in position and velocity were computed at every instant of time for the duration of the whole simulation.

Figs. 10 shows the results of the single parameter campaign. Besides the peculiar behaviour generated by the presence of eclipses, the general trend is that both the error in position and velocity increase as the values of the orbital

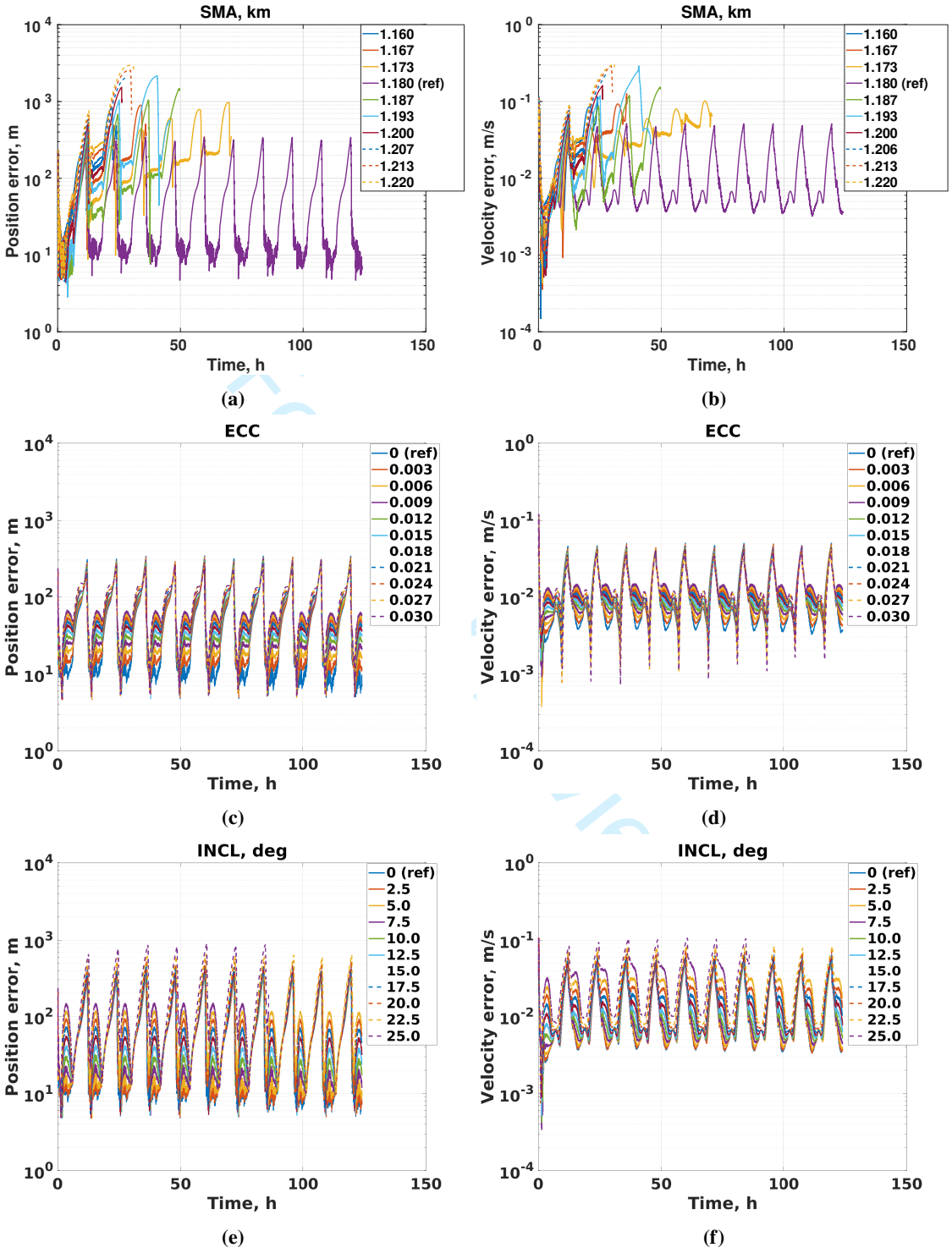

Fig. 10 Position and velocity estimation errors due to variations of the spacecraft's knowledge of the orbital parameters of the secondary asteroid with respect to the primary.

parameters get further from the nominal ones. Figs. 10a and b prove that the semi-major axis is a critical parameter. In fact a variation of the semi-major axis causes a variation of the orbital period. The variation in the orbital period causes the presence of long term and high amplitude periodic differences between the real position of the secondary asteroid and the one *believed* by the spacecraft. The period of these variations will be equal to the synodic period between the real orbital period of the secondary asteroid and the believed one. The amplitude can be as big as twice the distance between the asteroids, i.e. when the real position of the secondary asteroid and the presumed one are in opposition. The coupling between the semi-major axis and the orbital period is so important that left unchecked it causes all the simulations to end prematurely, with the spacecraft crashing on one of the two asteroids.

The other two orbital parameters, instead, cause an increase in the estimation error but in a less catastrophic way. This is because these two parameters do not induce changes in the period of the asteroid. Nevertheless, their perturbing effect is important as it makes the estimation error even one order of magnitude higher in this campaign.

Additional considerations can be made about the *shape* of the estimation error according to the variations of the different parameters. As long as the position error is concerned, it seems that, as the values of the semi-major axis go further away from the reference one, during the phases with presence of measurements the average error tends to increase in a *logarithmic* way, with smaller oscillations. The logarithmic slope is actually part of the long period sine function associated to the synodic period.

Regarding the effects of the inclination, it can be seen how a greater difference leads to oscillations of the mean value of the error with a greater amplitude. The evolution of the error resembles a sine function.

Finally, it seems that the eccentricity of the orbit plays a role similar to the inclination but the shape of the cusps is more skewed, with values of the error at the beginning of a new phase with measurements smaller than the ones closer to the beginning of the eclipses.

2. Multiple parameter analysis

A second analysis was performed to assess possible coupling effects when more parameters are varied at the same time. A total of 60 samples was generated using a Latin Hypercube Sampling (LHS) algorithm with values still bound by the ones of Table 2. Even in this case, for each combination of the orbital parameters values, 100 simulations were run and the mean on the error in position and velocity was computed.

Figs. 11 shows the outcome of this campaign. Out of 60 samples, only 4 survived until the end of the simulation. Their indices are reported in the figure and details about the respective values of semi-major axis, eccentricity and inclination deltas, relative to the reference values, are listed in Table 3, sorted according to increasing values of the estimation errors.

What comes immediately from the comparison of these surviving samples is that all of them have values of the orbital parameters quite close to the reference ones. Here, however, it is more difficult to identify parameter-specific

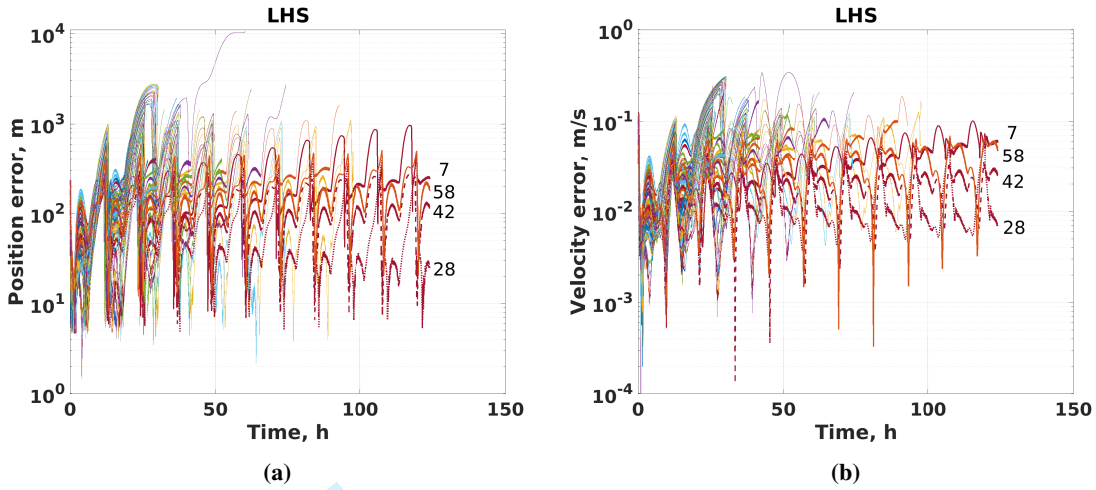

(a) (b)

Fig. 11 Position and velocity estimation errors due to simultaneous variations of the spacecraft's knowledge of the orbital parameters of the secondary asteroid with respect to the primary, generated through LHS.

Table 3 Values of semi-major axis, eccentricity and inclination deltas of the surviving samples

sample	ΔSMA, m	ΔECC	ΔINC, deg
28	0.4498	0.0227	4.4097
42	-0.9234	0.0241	11.6999
58	-1.3188	0.0296	18.6967
7	-3.3685	0.0168	2.5758

trends, as the values are closer together.

Nevertheless, it is still possible to identify peculiar behaviours. In fact, it seems that the position errors tend to follow a sort of linear trend, whose slope depends on the value of ΔSMA. Even in this case, however, such trend is just another expression of the sine function associated to the synodic period.

Longer simulations for these surviving samples, in fact, showed that samples 7, 58 and 42 will also eventually lead the spacecraft to crash on one of the asteroids. The position error of sample 28, instead, keeps decreasing for a short time until it starts increasing again, confirming the long scale periodic effects of the difference in semi-major axis.

It is clear that the uncertainty on the orbital parameters introduces perturbations that are difficult to predict and basically impossible to compensate by the current combination of measurements and filter. However, the most critical parameter remains the semi-major axis. In the following section an approach is presented to extend the applicability of the triangulation technique that includes the semi-major axis in the state estimation process.

VI. Augmented Triangulation Approach

From the analyses in the previous section it is apparent that an error in the estimation of the semi-major axis of the secondary can prevent the spacecraft from navigating properly. Thus, the idea is to add the estimation of the semi-major

axis to the estimation process. The estimated state is augmented including the semi-major axis of the orbit of the secondary asteroid around the primary and all the associated weight matrices are augmented accordingly. At first, no initial error was given to the semi-major axis and a small variance was assigned to it. Under these conditions no significant effects were present in the state estimation. Subsequently, the initial error and variance on the semi-major axis were increased. Figs. 12 show the estimation errors when the initial error on the semi-major axis is set to 9×10^{-4} km with variance 81×10^{-8} km^2. The error on the estimated quantities generally increases after every orbit and eventually becomes so large that the behaviour would become chaotic. The spacecraft would end up crashing onto the asteroids or escaping the binary system. The critical condition occurs when, during an eclipse, the spacecraft has drifted so far from L4 that it enters the region of space of L5 when the Sun appears again on the side of L4. When this happens, generally after 60h, the eclipse does not end when supposed to but the spacecraft continues navigating without measurements until it will find itself again on the same half-plane where the Sun is. In some cases, indeed, this condition does not occur after 60h and the spacecraft survives until the end of the simulation.

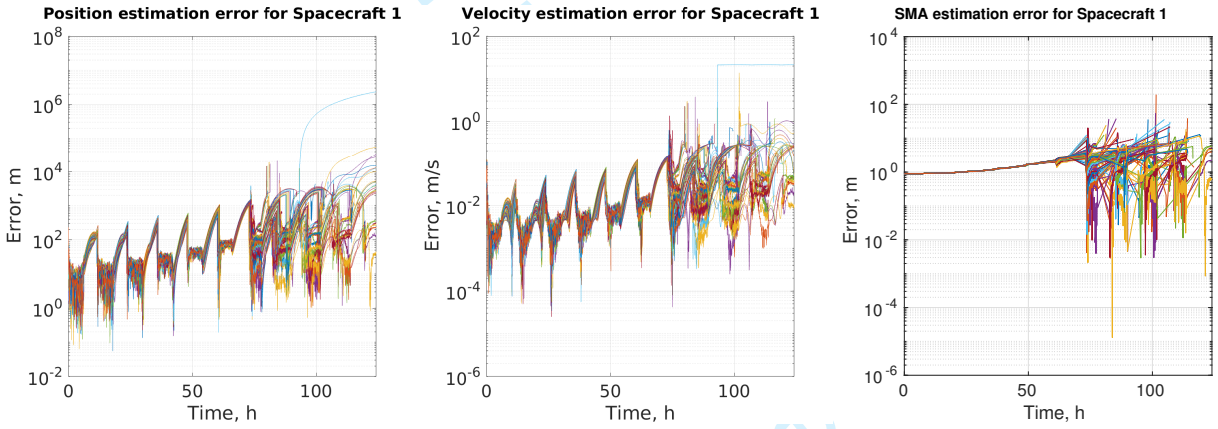

Fig. 12 Estimation errors when estimating the SMA of the secondary asteroid's orbit using the basic triangulation technique.

A. Single Spacecraft Navigation Strategy

It is hence necessary to provide more information to the system to try to correctly bound the estimated values of the semi-major axis. The major challenge is to achieve this goal without the use of additional sensors.

The most natural approach comes still from the triangulation method. So far it has only been used to obtain the position of the spacecraft relative to the primary asteroid. Nevertheless, from equation (12), once the value $\|\mathbf{r}_{AC_i}\|$ is found, the value $\|\mathbf{r}_{BC_i}\|$, can be trivially obtained from:

$$\|\mathbf{r}_{BC_i}\| = \frac{sin(\alpha_{iA})}{sin(\alpha_{iB} - \alpha_{iA})}\|\mathbf{r}_{AB}\| = \frac{sin(\alpha_{iA})}{sin(\alpha_{iB})}\|\mathbf{r}_{AC_i}\| \tag{25}$$

This distance, together with the pointing vector coming from the cameras, yields the relative position vector between the spacecraft and the secondary asteroid, thus providing information about the position of the secondary asteroid. The resulting new measurement consists of the values of Eq. (13) together with the ones of Eq. (25). This measurement augmentation strategy is first tested applying no initial error to the semi-major axis and assigning a 6x6 diagonal weight matrix to the measurement, with values equal to 9×10^{-4} km^2. Fig. 13 shows the evolution of the system for one of the 100 runs performed, while Figs. 14 report the mean values for the estimation errors and the 1-σ uncertainties for this test case. These results are satisfactory because the position and velocity errors are similar to the ones previously obtained when assuming a perfect knowledge of the motion of the secondary asteroid. The error in position is around 10 m and never exceeds 30 m. This is allowed by the fact that now the filter manages to bound the value of the estimated semi-major axis whose error, after an initial raise, stabilises and stays around 0.1 m.

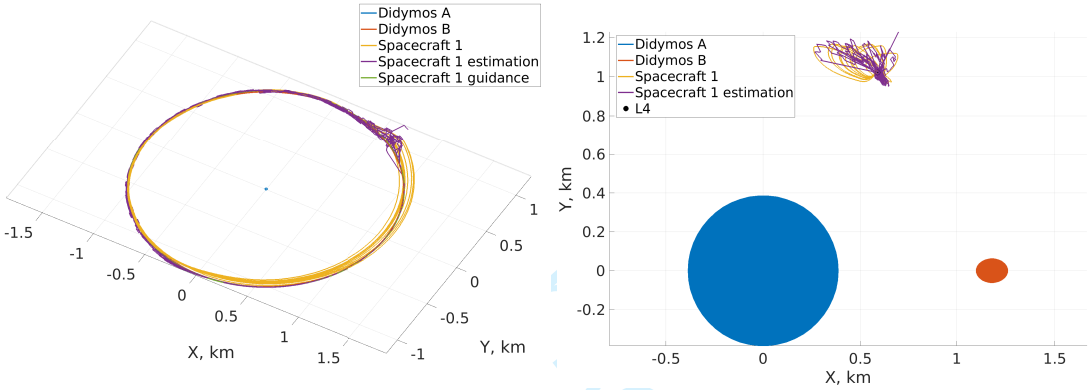

(a) Non-rotating frame **(b) Rotating frame**

Fig. 13 Real, guidance and navigation trajectories of the spacecraft when estimating the SMA of the secondary asteroid's orbit using the augmented triangulation technique. No initial error on SMA.

The performance of the augmented measurement was further investigated with a test case where the initial error on the knowledge of the semi-major axis was set to the maximum value used during the sensitivity analysis, 40 m, and the errors on eccentricity and inclination were set to those of the surviving sample number 28, Table 3. This required some tuning of the weight matrix associated to the measurements that, once set to a diagonal matrix whose first three elements - the ones associated to the relative position of the spacecraft to the primary asteroid - set to 9×10^{-2} km^2 and the last three - associated to the relative position to the secondary asteroid - set to 36×10^{-4} km^2, produce the results shown in Figs. 15 and 16. Even for this test case a set of 100 simulations was run. In this scenario the filter takes longer to converge, given the relatively high error on the semi-major axis, hence the activation of the controller is delayed until 24 hours have passed, i.e. slightly more than two orbital periods of the binaries. After this long transient, the error on the semi-major axis stabilises and reaches values lower than 1 m. Importantly, both the position and velocity errors remain stable for the whole simulation, with the position error being around 100 m. The position error in this case is almost one order of magnitude higher than in the previous case but this is essentially due to the presence of uncertainty

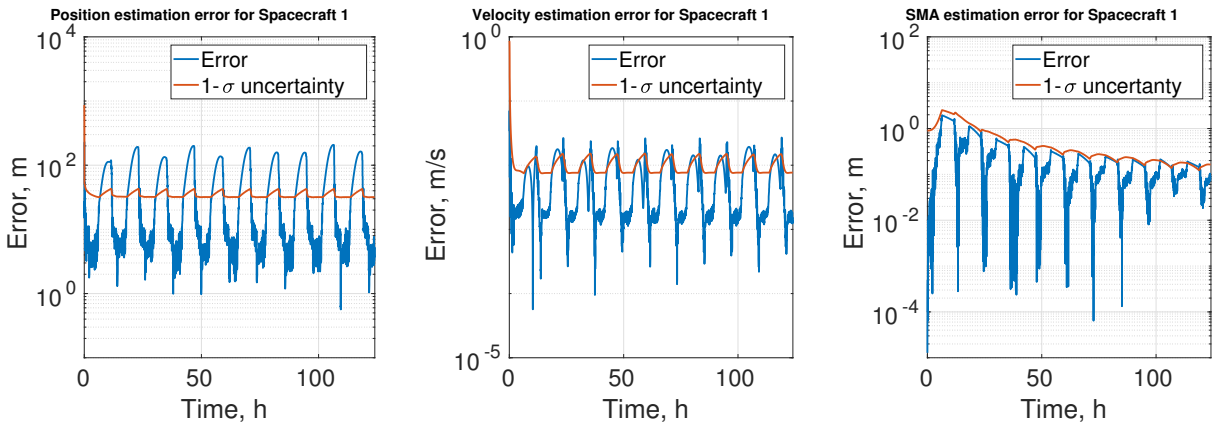

Fig. 14 Estimation errors when estimating the SMA of the secondary asteroid's orbit using the augmented triangulation technique. No initial error on SMA.

on 3 different orbital parameters and the lower reliability of the measurements dictated by the elements of its associated weight matrix. The most important achievement is that all the errors are stable and no divergence occurs. This means

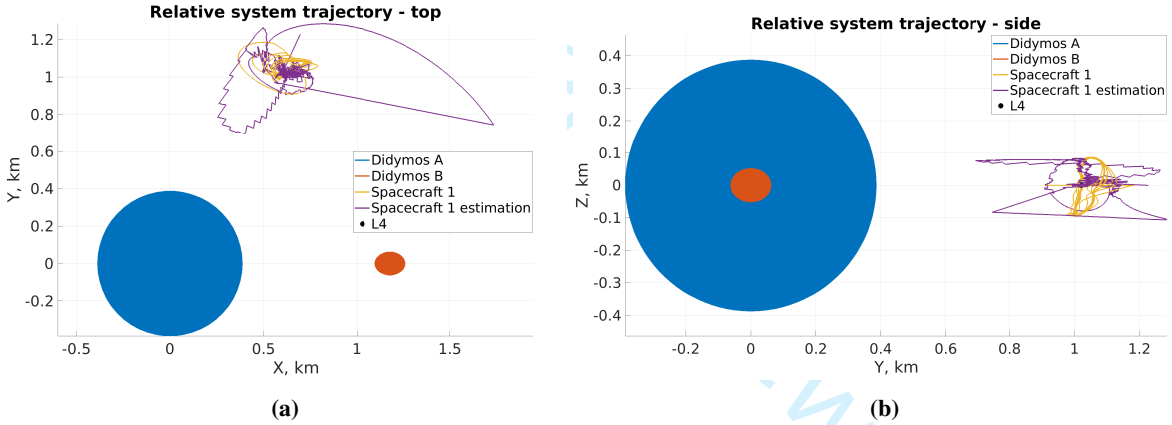

Fig. 15 Real, guidance and navigation trajectories of the spacecraft when estimating the SMA of the secondary asteroid's orbit using the augmented triangulation technique. Initial error on SMA = 40 m.

that the proposed measurement augmentation is capable of compensating uncertainties on the value of the semi-major axis of the orbit of the secondary asteroid, at least within the range used as a reference in this work.

B. Two Spacecraft Formation

In this section a further scenario is investigated in which two identical spacecraft need to navigate at L4. In this new scenario, both spacecraft are provided with the inter-spacecraft measurement described in Section III.D. In a previous work it was demonstrated that the use of the relative position vector could improve the estimation process and also allow a spacecraft to continue navigating even when the cameras became unavailable [26].

The goal of this scenario is to assess the effects of the use of the inter-spacecraft communication when the spacecraft

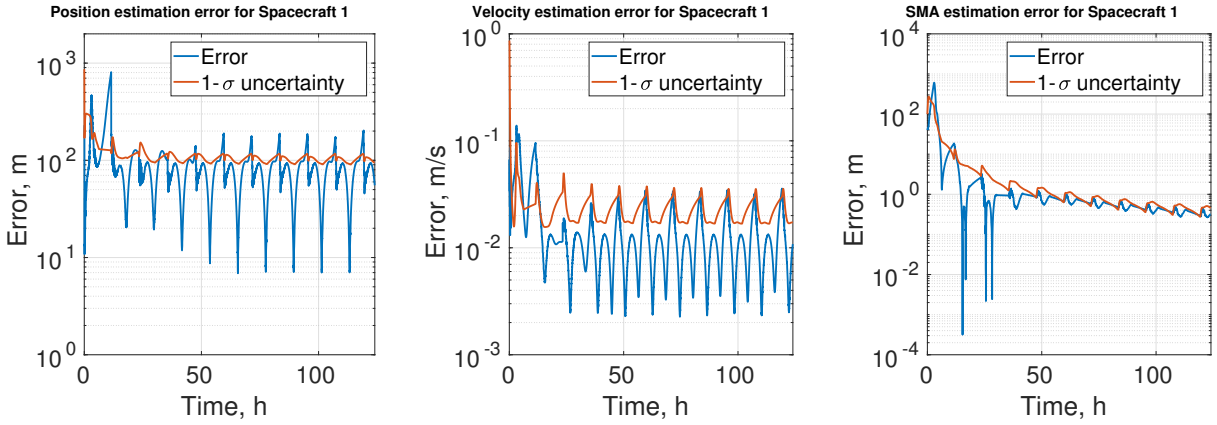

Fig. 16 Estimation errors when estimating the SMA of the secondary asteroid's orbit using the augmented triangulation technique. Initial error on SMA = 40 m.

are estimating also the semi-major axis of the secondary asteroid. It is important to recall how the timing between the measurements was set in the previous work, outlined in Figure 17. In a scenario with two spacecraft, both spacecraft would take a measurement from the cameras every 10 minutes, with the difference that one of the two would take its measurements with a delay of 5 minutes. This guarantees that there is a camera-based measurement available every 5 minutes in one of the spacecraft. Consider the case in which Spacecraft 1 takes the measurements and performs a new estimation of its own state. Immediately after, this new value is transmitted to Spacecraft 2. At the time of reception of the signal, Spacecraft 2 uses this information and the relative position measurement to perform a new estimation of its own state. This is then transmitted to Spacecraft 1 that would perform a new estimation of its state based on the relative position measurement. At this point, Spacecraft 1 checks how much time is passed from the last transmission of its own state and decides whether to transmit or not according to a minimum time threshold. This is crucial to avoid a continuous exchange of information between the spacecraft. The result of this strategy is that each spacecraft performs two state estimations, the first one camera-based and the second one relative position-based, in a very short time, followed by another relative position-based one after roughly 5 minutes, before starting a new cycle again with a new camera-based estimation.

This strategy would not work when the spacecraft also estimate other parameters besides their own state. It has been already shown in Section III.C that the simple triangulation technique is not enough under these conditions and that an augmentation method is necessary because of the increased length of the state to estimate. For the same reason, a simple relative position measurement would not be enough to bound the estimation process, given that no information can be extracted about the value of the semi-major axis of the motion of the secondary asteroid. Two possible solutions can be considered to tackle this issue: one is to add more measurements, trying to provide more information to each spacecraft when the cameras are not used; another one is to synchronise the use of both the cameras and the relative position sensor

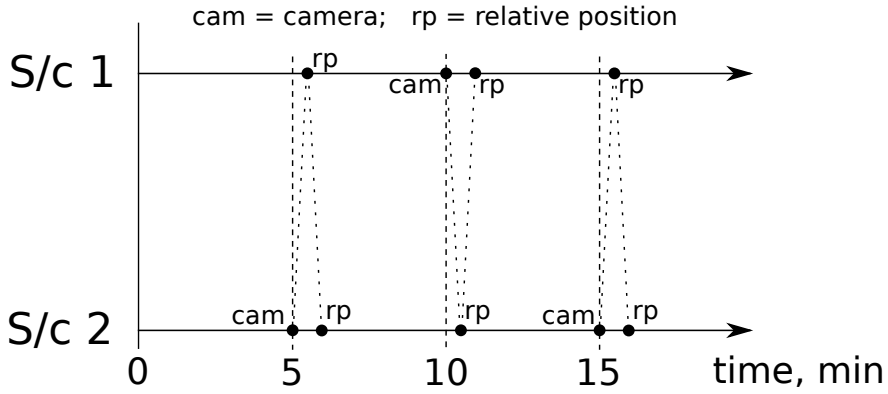

Fig. 17 Asynchronous scheme for measurement timing and information sharing between two spacecraft.

with the reception of the signal from the other spacecraft. The former solution would most likely require additional sensors and is therefore discarded. The latter solution is a simple modification to the timing strategy proposed in this section, with the communication scheme remaining unchanged. As can be seen in Fig. 18, each spacecraft will have the information coming from the augmented triangulation and the relative position sensor almost at every estimation. The only exception is the first measurement of every time interval, when only the augmented triangulation is available.

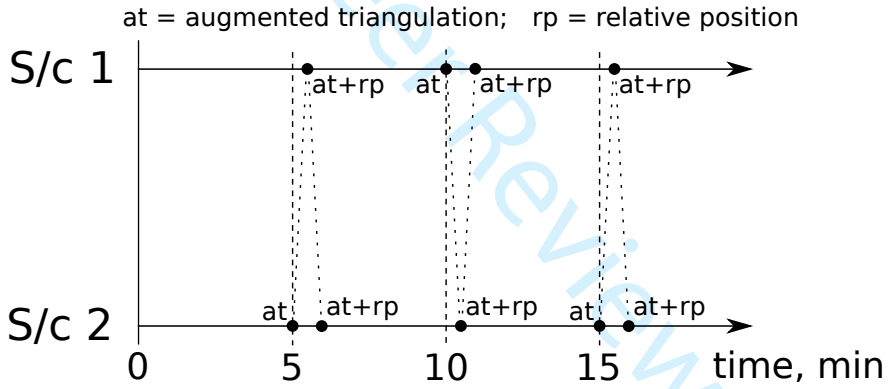

Fig. 18 Synchronous scheme for measurement timing and information sharing between two spacecraft.

Figures 19 and 20 show the results of a possible two spacecraft scenario. The two identical spacecraft are tasked to maintain their position in the proximity of two different locations situated close to L4. Spacecraft 1 chases a point located at $-5°$ from the position of L4, while Spacecraft 2 chases a location at $+5°$ deg from L4. The relative position sensors are affected by a zero mean Gaussian noise having standard deviation equal to 2 m in range and 10^{-3} rad in azimuth and elevation. The weight matrices associated to the relative position measurements are 3×3 diagonal matrices with all the elements equal to 4×10^{-2} km^2. This value is very close to the one assigned to the triangulation measurement and it means that the same degree of reliability is assigned to both the sets of information. In fact, even though the relative position measurement itself has a higher precision that the one achievable by the triangulation method, its contribution to the estimation process depends on the information transmitted by each spacecraft. This one is indeed affected by the

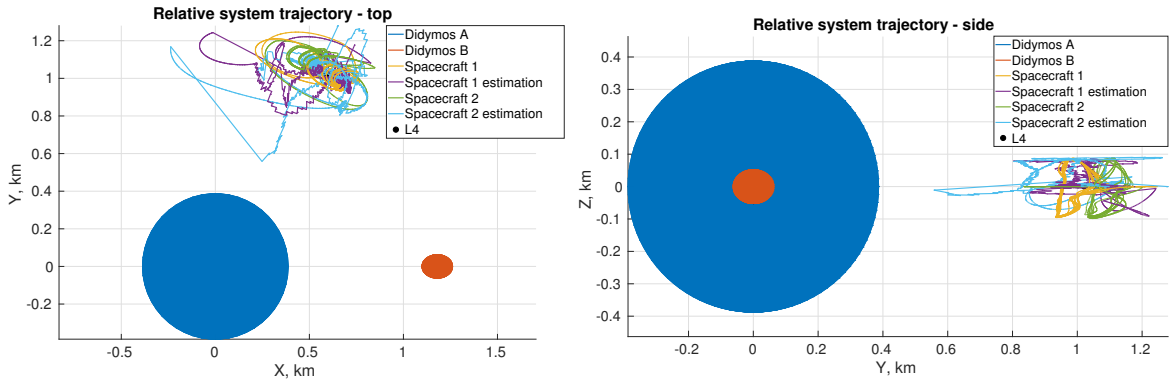

(a) (b)

Fig. 19 Real, guidance and navigation trajectories of the two spacecraft when estimating the SMA of the secondary asteroid's orbit using the inter-spacecraft communication.

lower reliability of the triangulation, thus limiting the reliability of the relative position measurements.

The estimation errors of both the spacecraft are consistent and similar to the ones obtained for the single spacecraft case in Section VI.A. The position estimation errors, when measurements are available, remain confined within 100 m, the velocity within 3 cm/s and the estimation of the SMA of the orbit of the secondary asteroid reach values lower than 1 m. As expected, the use of the inter-spacecraft link is not producing significant effects on the state estimation. The only visible effect is the apparent thickening of the estimated $1-\sigma$ uncertainty line when not in eclipse, that is actually a high frequency oscillation of its values. In general, in fact, the estimated uncertainty computed using the relative position measurement is slightly smaller than the one obtainable when only the augmented triangulation is used. Figs. 21 shows the relative distance between the spacecraft, real and estimated, during the whole simulation and the error between the two. After the two orbital periods without control, where the maximum distance goes up to 630 m, the real relative distance between the spacecraft remains at about 210 m. All those arcs where the distance changes occur during the eclipses, with the minimum distance never getting lower than 50 m. The estimated relative distance is obtained by comparing the estimated states of the two spacecraft. The greatest differences again occur during the eclipses, when no measurements are produced by the cameras. In presence of measurements, instead, the error on the estimated inter-spacecraft distance is within 40 m at the end of the eclipses and remains below 10 m until a new eclipse begins.

C. Failure Analysis

In this last test case, the effect of malfunctioning cameras on the estimation process is investigated, similarly to what already presented in a previous work [26]. The scenario starts as in the previous test case. At a certain point, at the completion of the 4^{th} orbit of the secondary asteroid, the cameras on Spacecraft 2 experience a total failure. In this way, Spacecraft 2 can only rely on the inter-spacecraft measurements to estimate its own state. A new estimation is performed only when new information is received from Spacecraft 1 hence, given the frequency of the measurements used in

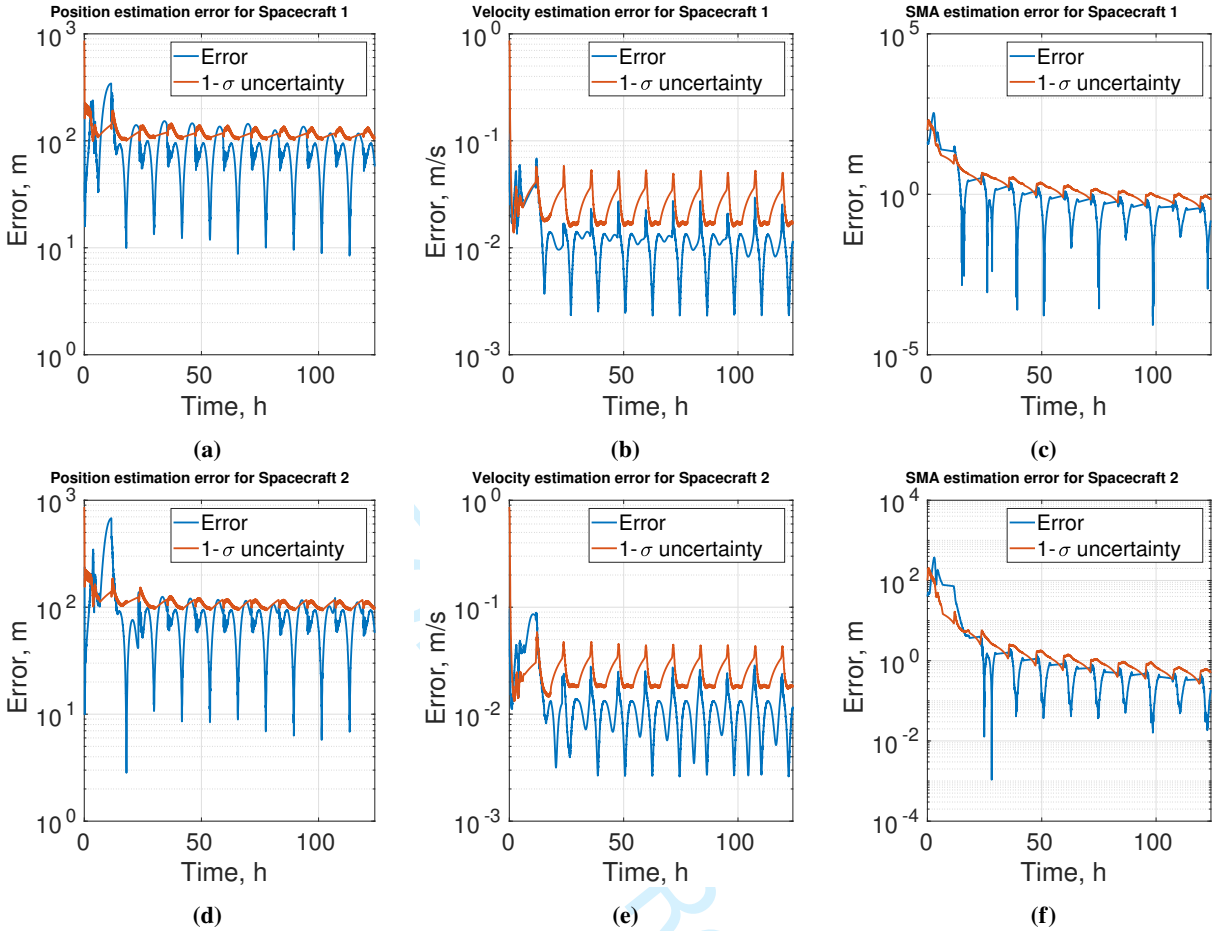

Fig. 20 Estimation errors of the two spacecraft when using inter-spacecraft communication.

the previous case, roughly every 10 minutes, as shown in Fig. 22. It is important to note that, as the cameras switch off, Spacecraft 2 will need to stop estimating the semi-major axis of the orbit of the secondary asteroid as previously explained. Nevertheless, its knowledge will still be required in the propagation of the sigma points of the filter, hence new updates on the Keplerian elements of the secondary asteroid will be provided by Spacecraft 1. One last remark is that, once the cameras switch off, the elements on the diagonal of the weight matrix associated to the relative position measurements on Spacecraft 2 are set to 64×10^{-4} km^2.

The results of this test case are presented in Figs. 23 and 24. As expected, as long as the cameras on Spacecraft 2 provide measurements, the evolution of the trajectories and the estimation errors resemble the one of the previous test case. After 4 orbital periods of the system, at about 48 hours, the cameras on Spacecraft 2 turn off and the estimation of the semi-major axis of the secondary asteroid on Spacecraft 2 stops as well. The rest of the simulation, as long as the estimation errors in position and velocity are concerned, proceeds quite similarly to the previous phase. The most evident proof of the absence of the cameras on Spacecraft 2 is the end of the oscillations of the values of the position and velocity uncertainties, that are still present for Spacecraft 1 instead. Two features stand out in this second part of

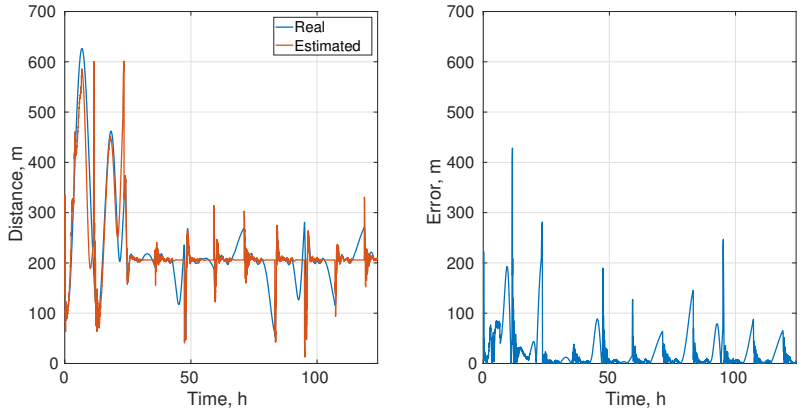

(a) (b)

Fig. 21 Real and relative distance and error between the two spacecraft when using inter-spacecraft communication.

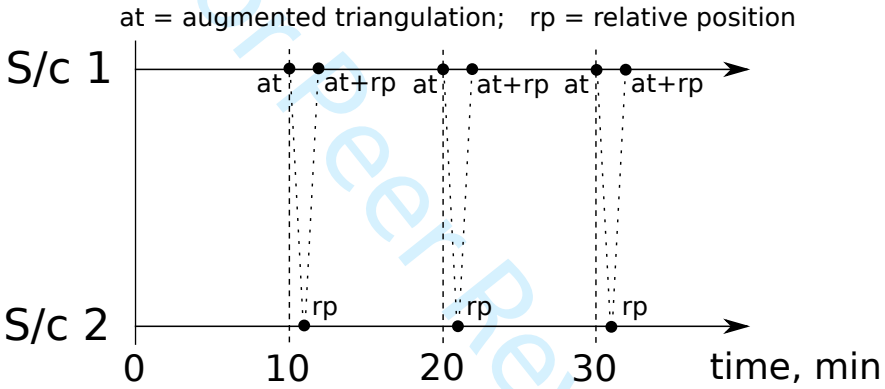

Fig. 22 Measurement timing and information sharing between two spacecraft with no cameras on Spacecraft 2.

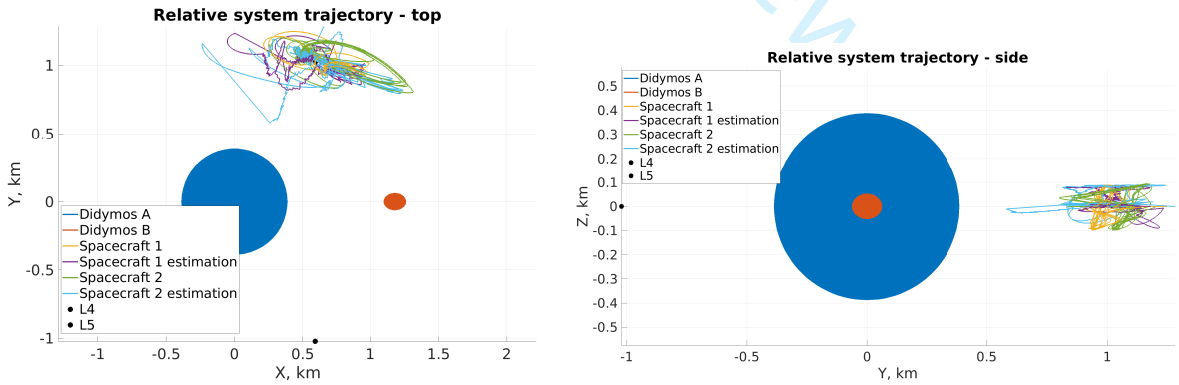

(a) (b)

Fig. 23 Real, guidance and navigation trajectories of the two spacecraft when the cameras on Spacecraft 2 are not working.

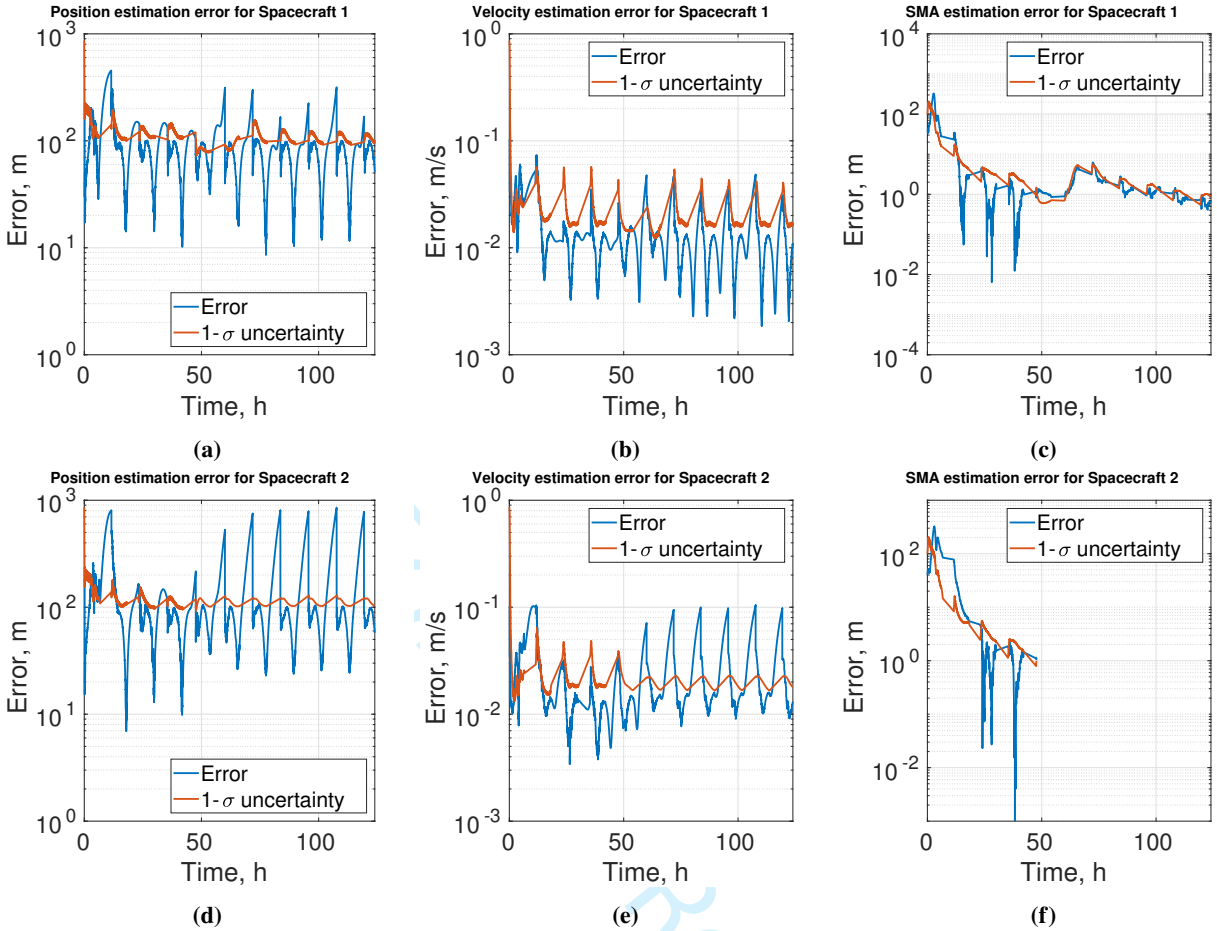

Fig. 24 Estimation errors of the two spacecraft when the cameras on Spacecraft 2 are not working.

the simulation. The first one is the greater propagation errors in the absence of measurements for Spacecraft 2. The second one is a variation in the pattern of the estimated position uncertainty of Spacecraft 1 during the orbital period immediately after the cameras switch off on Spacecraft 1. Both these behaviours can be explained by the effects of the loss of the cameras on the estimation of the semi-major axis of the orbit of the secondary asteroid and the overall lower frequency of the measurements. It can be seen that, immediately after the loss of the cameras, during the first orbital period the estimation error on the semi-major axis stays almost constant but above the estimation uncertainty. After the following eclipse time, there is a steep increase in both error and uncertainty, as the filter on Spacecraft 1 tries to compensate the loss of information. Then the estimation error starts decreasing steadily again, reaching pre-camera-loss values by the end of the simulation. A higher error on the estimation of the semi-major axis produces greater errors in the propagated states and in the performance of the triangulation sensor. Even in this test case, Figs. 25 show the relative position between the two spacecraft. The general behaviour is similar to the one obtained in the previous scenario, with only higher spikes occurring during and at the end of eclipse phases.

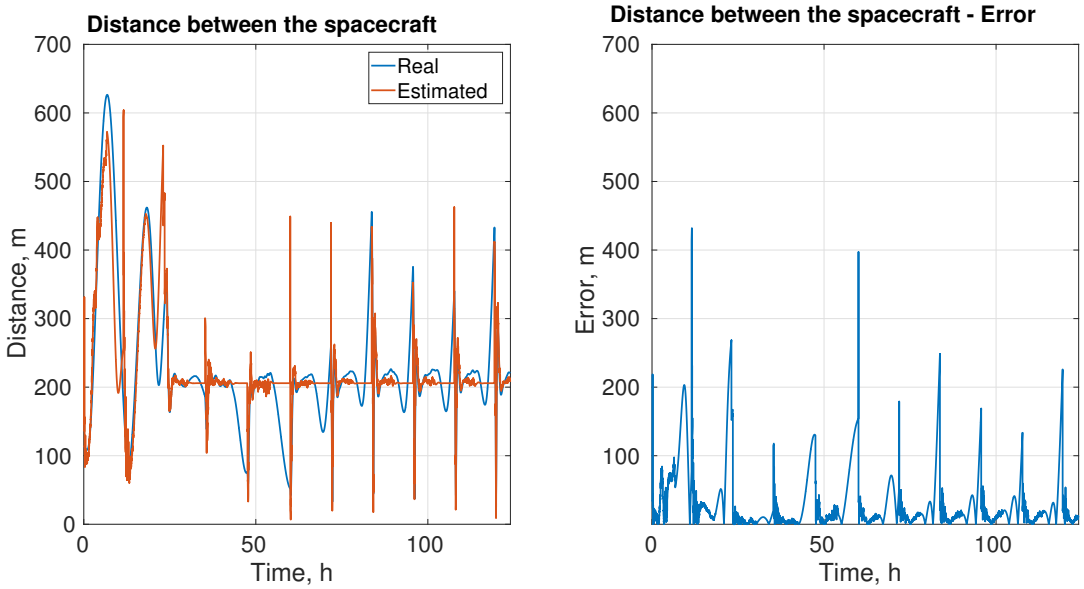

Fig. 25 Real and relative distance and error between the two spacecraft when the cameras on Spacecraft 2 are not working.

VII. Conclusions

This paper investigated the autonomous navigation of a small formation of spacecraft in the proximity of the Lagrangian point L4 of a binary asteroid system using camera-based angles-only measurements and some knowledge of the dynamical evolution of the environment.

A triangulation method was proposed to obtain an expression of the state of the spacecraft and it provided satisfactory performance. However, its critical dependence on the knowledge of the evolution of the dynamical system was identified and investigated. The results showed that the most critical parameter is the semi-major axis of the orbit of the secondary asteroid as it induces long term variations between the real state of the secondary asteroid and the one predicted by the spacecraft with period equal to the synodical period between them.

A method to augment the information provided by the triangulation was proposed to allow the spacecraft to estimate the value of the semi-major axis of the orbital motion of the secondary asteroid. This method allows the spacecraft to safely navigate even with some residual uncertainty on some of the other orbital parameters.

In the presence of a second identical spacecraft, the use of inter-spacecraft communication with the augmented triangulation did not lead to particular improvements in the estimation errors. This conclusion is, however, applicable only to the settings analysed in this paper. More work is required to draw more general conclusions on the applicability of this data fusion concept to a general case. In the case where the cameras fail on one of the spacecraft, it was proven that the spacecraft experiencing the failure is still capable of autonomously navigating using only the inter-spacecraft communication and relative position measurements, as long as the other spacecraft provides the necessary additional

information.

The assumptions used in this paper on the relative position of spacecraft and asteroids restrict the applicability of the image processing algorithm only to the case of a relative navigation at one of the triangular Lagrangian points. Nonetheless, the navigation concept and measurement strategy can be extended to other navigation scenarios provided that the image processing algorithm can extract the required information, namely the pointing vectors and the relative positions of the two asteroids. This extension will be the subject of future work. Further developments are also required to treat cases in which the shape of the asteroids is more irregular than what considered in this paper. In this case a simple limb fitting algorithm might not be sufficient to provide the required information.

References

[1] Coradini, A., Turrini, D., Federico, C., and Magni, G., "Vesta and Ceres: Crossing the History of the Solar System," *Space Science Reviews*, Vol. 163, No. 1, 2011, pp. 25–40. doi:10.1007/s11214-011-9792-x, URL `https://doi.org/10.1007/s11214-011-9792-x`.

[2] Margot, J. L., and Nolan, M. C. e. a., "Binary Asteroids in the Near-Earth Object Population," *Science*, Vol. 296, No. 5572, 2002, pp. 1445–1448. doi:https://doi.org/10.1126/science.1072094.

[3] Cheng, A., and Rivkin, A. e. a., "Binary and Multiple Systems," 2009.

[4] Champetier, C., Regnier, P., Serrano, J., and De Lafontaine, J., "Evaluation of Autonomous GNC Strategies for the Roseti a Interplanetary Mission1," *IFAC Proceedings Volumes*, Vol. 25, No. 22, 1992, pp. 339–353.

[5] De Lafontaine, J., "Autonomous spacecraft navigation and control for comet landing," *Journal of Guidance, Control, and Dynamics*, Vol. 15, No. 3, 1992, pp. 567–576.

[6] Kawaguchi, J. I., Hashimoto, T., Kubota, T., Sawai, S., and Fujii, G., "Autonomous Optical Guidance and Navigation Strategy Around a Small Body," *Journal of Guidance, Control, and Dynamics*, Vol. 20, No. 5, 1997, pp. 1010–1017.

[7] Owen, T. C., W. M. Jr.and Wang, Harch, A., Bell, M., and Peterson, C., "NEAR optical navigation at Eros," *AAS/AIAA Astrodynamics Specialist Confrerence*, AAS, Quebec City, Canada, July 30-August 2, 2001.

[8] Getzandanner, K. M., "Navigation Strategies for Primitive Solar System Body Rendezvous and Proximity Operations," *AAS/AIAA Astrodynamics Specialist Confrerence*, AAS, Quebec City, Canada, July 30-August 2, 2001.

[9] Scheeres, D., "Close proximity operations for implementing mitigation strategies," *2004 Planetary Defense Conference: Protecting Earth from Asteroids*, 2004, p. 1445.

[10] Broschart, S. B., and Scheeres, D. J., "Control of Hovering Spacecraft Near Small Bodies: Application to Asteroid 25143 Itokawa," *Journal of Guidance, Control, and Dynamics*, Vol. 28, No. 2, 2005, pp. 343–354.

[11] Li, W., and Jia, Y., "H-infinity filtering for a class of nonlinear discrete-time systems based on unscented transform," *Signal Processing*, Vol. 90, No. 12, 2010, pp. 3301–3307. doi:https://doi.org/10.1016/j.sigpro.2010.05.023.

[12] Llanos, P. J., Di Domenico†, M., and Gil-Fernandez‡, J., "Advanced GNC Technologies for Proximity Operations in Missions to Small Bodies," *15th Reinventing Space Conference*, AAS, Glasgow, UK, 2013.

[13] Jiang, X., Tao, T., Yang, W., and Li, S., "GNC schemes design for future China asteroid exploration," *34th Chinese Control Conference (CCC), Hangzhou, China*, 2015. doi:https://doi.org/10.1109/ChiCC.2015.7260458.

[14] S. Hesar, J. M., J. Parker, and Born, G., "Small Body Gravity Field Estimation Using LIAISON Suplemented Optical Navigation," *AAS GN&C Conference*, 2015.

[15] K. Fujimoto, N. S., and Turner, J. M., "Stereoscopic Image Velocimetry as a Measurement Type for Autonomous Asteroid Gravimetry," *American Institute of Aeronautics and Astronautics*, 2016.

[16] Vetrisano, M., and Vasile, M., "Autonomous Navigation of a Spacecraft Formation in the Proximity of an Asteroid," *Advances in Space Research*, Vol. 57, No. 8, 2016, pp. 1783–1804. doi:https://doi.org/10.1016/j.asr.2015.07.024.

[17] Torre, F., Vasile, M., Serra, R., and Grey, S., "Autonomous Navigation of a Formation of Spacecraft in the Proximity of a Binary Asteroid," *ISTS 2017, Ehime, Japan*, 2017.

[18] N., S., and S., D., "Autonomous Swarming for Simultaneous Navigation and Asteroid Characterization," *2018 AAS/AIAA Astrodynamics Specialist Conference*, AAS, Snowbird, UT, USA, August 19-23, 2018.

[19] Christian, J. A., and Lightsey, G. E., "Onboard Image-Processing Algorithm for a Spacecraft Optical Navigation Sensor System," *Journal of Spacecraft and Rockets*, Vol. 49, No. 2, 2012, pp. 337–352. doi:https://doi.org/10.2514/1.A32065.

[20] Bhaskaran, S., and Kennedy, B., "Terminal Guidance Navigation for an Asteroid Impactor Spacecraft," *23rd AAS/AIAA Spaceflight Mechanics Meeting, Kauai, HI, United States*, 2013. doi:http://hdl.handle.net/2014/44056.

[21] Yang, H., Yang, X., and Zhang, W., "State Estimation of Spacecraft Formation near Small Asteroid," *IEEE Chinese Guidance, Navigation and Control Conference, Yantai, China*, 2014. doi:https://doi.org/10.1109/CGNCC.2014.7007219.

[22] Gil-Fernandez, J., and Ortega-Hernando, G., "Autonomous vision-based navigation for proximity operations around binary asteroids," *CEAS Space Journal*, Vol. 10, No. 2, 2018, pp. 287–294. doi:https://doi.org/10.1007/s12567-018-0197-5.

[23] Stastny, N. B., and Geller, D. K., "Autonomous Optical Navigation at Jupiter: A Linear Covariance Analysis," *Journal of Spacecraft and Rockets*, Vol. 45, No. 2, 2008, pp. 290–298. doi:https://doi.org/10.2514/1.28451.

[24] Manghi, R. L., Modenini, D., Zannoni, M., and Tortora, P., "Preliminary orbital analysis for a CubeSat mission to the Didymos binary asteroid system," *Advances in Space Research*, 2017. doi:https://doi.org/10.1016/j.asr.2017.12.014, URL `http://www.sciencedirect.com/science/article/pii/S0273117717308906`.

[25] Vetrisano, M., Colombo, C., and Vasile, M., "Asteroid Rotation and Orbit Control via Laser Ablation," *Advances in Space Research*, Vol. 57, No. 8, 2016, pp. 1762–1782. doi:https://doi.org/10.1016/j.asr.2015.06.035.

[26] Torre, F., Serra, R., Grey, S., and Vasile, M., "Angles-Only Navigation of a Formation in the Proximity of a Binary System," *AIAA SciTech Forum, Kissimmee, FL, USA*, 2018. doi:https://doi.org/10.2514/6.2018-1976.

[27] Thiry, N., and Vasile, M., "Binary Asteroid Manipulation with Laser Ablation," *HPLA/DE, Santa Fe, 4-6 April 2016*, 2016.

[28] Vasile, M., and Thiry, N., "LightTouch3: a demo mission to test laser ablation for asteroid manipulation and exploitation," *15th Reinventing Space Conference*, BIS, Glasgow, UK, 24-26 October 2017.

[29] Scheeres, D. J., "Orbit Mechanics about Asteroids and Comets," *Journal of Guidance, Control and Dynamics*, Vol. 35, No. 3, 2012, pp. 987–997. doi:https://doi.org/10.2514/1.57247.

[30] Hu, W., and Scheeres, D. J., "Spacecraft motion about slowly rotating asteroids," *Journal of Guidance, Control and Dynamics*, Vol. 25, No. 4, 2002, pp. 765–775. doi:https://doi.org/10.2514/2.4944.

[31] Li, S., Cui, P. Y., and Cui, H. T., "Vision-aided inertial navigation for pinpoint planetary landing," *Aerospace Science and Technology*, Vol. 11, No. 4, 2007, pp. 499–506. doi:https://doi.org/10.1016/j.ast.2007.04.006.

[32] Thevenet, J.-B., and Grelier, T., "Formation Flying Radio-Frequency metrology validation and performance: The PRISMA case," *Acta Astronautica*, Vol. 82, No. 1, 2013, pp. 2 – 15. doi:https://doi.org/10.1016/j.actaastro.2012.07.034, URL `http://www.sciencedirect.com/science/article/pii/S0094576512002998`, 6th International Workshop on Satellite Constellation and Formation Flying.

[33] Vasile, M., Torre, F., Serra, R., and Grey, S., "Autonomous orbit determination for formations of Cubesats beyond LEO," *Acta Astronautica*, Vol. 153, 2018, pp. 327 – 336. doi:https://doi.org/10.1016/j.actaastro.2018.01.045, URL `http://www.sciencedirect.com/science/article/pii/S0094576517314728`.

[34] Alonso, R., Du, J., and Hughes, Y., "Relative Navigation for Formation Flying of Spacecraft," *Proceedings of the Flight Mechanics Symposium, NASA-Goddard Space Flight Center, Greenbelt, MD*, 2001, pp. 115–129.

[35] Julier, S. J., Uhlmann, J. K., and Durrant-Whyte, H. F., "A new approach for filtering nonlinear systems," *American Control Conference*, IEEE, Seattle, WA, 1995, pp. 1628, 1632.

[36] Michel, P. e. a., "Science case for the Asteroid Impact Mission (AIM): A component of the Asteroid Impact & Deflection Assessment (AIDA) mission," *Advances in Space Research*, Vol. 57, No. 12, 2016, pp. 2529–2547. doi:https://doi.org/10.1016/j.asr.2016.03.031.